THESIS

PROCESSING OF MAYENITE ELECTRIDE AND ITS COMPOSITES IN SPARK PLASMA SINTERING

Submitted by

Adam Edward Kuehster

School of Advanced Materials Discovery

In partial fulfillment of the requirements

For the Degree of Master of Science

Colorado State University

Fort Collins, Colorado

Summer 2019

Master's Committee:

Advisor: Kaka Ma

Chris Weinberger
John Williams

ABSTRACT

PROCESSING OF MAYENITE ELECTRIDE AND ITS COMPOSITES IN SPARK PLASMA SINTERING

Mayenite electride, as the first inorganic room temperature stable electride, has attracted intensive research interests since the early 2000s due to its great potential in various applications such as catalysts, conductive oxides and thermionic emission materials. Mayenite electride is developed from mayenite, a stoichiometric compound of CaO and Al_2O_3 ($12CaO{\cdot}7Al_2O_3$, referred to as C12A7 hereafter) that has a cubic unit cell with a positively charged lattice framework $[Ca_{24}Al_{28}O_{64}]^{4+}$ of twelve crystallographic subnano-cages per unit and O^{2-} anions clathrated in the cages to maintain charge neutrality. When C12A7 is heat treated in a reducing environment, electrons replace O^{2-} ions clathrated in the cages. The electrons can migrate through the inter-cage framework, leading to the formation of electride (C12A7:e^-), an electrically conductive form of C12A7. A variety of methods to make C12A7:e^- powder and bulk materials have been investigated in the literature, all of which involve multiple steps and long-time (days to weeks) of heat treatment at high temperatures (>1100 ˚C). Although fundamental knowledge of the structure and functionality of C12A7:e^- is advancing in the field, the formation of other calcium aluminate phases during the synthesis of C12A7 or its electride has been overlooked. Most of the previous studies also lack detailed microstructure characterization. In addition, monolithic C12A7:e^- does not provide continuous ohmic contact due to the destruction of the surface cages during processing, which limits its direct use in thermionic emission devices. To address the aforementioned practical issues and to fill in the fundamental knowledge gap, we investigated the effect of adding different

reinforcing particles, including carbon black (CB), Ti, and TiB_2, on the formation of C12A7:e^- via spark plasma sintering (SPS), with attention particularly paid to address phase formation during the processing. Specifically, preformed C12A7 powder was synthesized via a solid-state reaction and used as the precursor base in SPS to study the effect of additives. In addition, a novel approach using *in-situ* reaction in SPS was proposed in the present work to significantly reduce the processing time.

My research revealed that both Ti and TiB_2 effectively reduced C12A7 to its electride phase, C12A7:e^-. However, addition of Ti and TiB_2 also led to partial decomposition of C12A7 into secondary calcium aluminate phases, primarily Al_2O_3-rich calcium monoaluminate (CA) and CaO-rich tricalcium aluminate (C3A). Although CB did not effectively reduce C12A7 to C12A7:e^-. it did not result in the formation of any secondary calcium aluminate phases. Using Ti foils on the top and bottom of the preformed C12A7 powder in SPS created C12A7:e^- with a near-theoretical maximum electron concentration ~ $10^{21}/\mathrm{cm}^3$. For the *in-situ* reaction approach, the chemical homogeneity and size distribution of precursor powders are critical to forming C12A7:e^- in the typical processing time frame of SPS (5-15 minutes). The fast heating rate and C-rich environment in SPS increased the $CaCO_3$ decomposition temperature to above 930°C, which is consequential to the calcium aluminate formation reaction. Adding Ti powder lowered the $CaCO_3$ decomposition temperature in SPS and allowed for the formation of C12A7:e^- via *in-situ* reaction sintering. The work function of a 50-50wt% C12A7:e^--Ti composite in this study is ~ 2.6 eV.

ACKNOWLEDGEMENTS

I would like to first thank my advisor Dr. Kaka Ma. Her guidance has been invaluable over the past two years, and I am truly proud to be her student. She will always be a role model as a researcher and a leader. I would also like to thank Dr. John Williams for his time spent in review of my graduate work. Dr. Chris Weinberger has also played an important role in my graduate education. Discussions with him about general education have been both insightful and entertaining. Dr. Donald Radford has also provided a great deal of assistance during my time at The Factory, for which I am grateful. I would also like to thank Dr. Troy Holland for starting me on this path.

I would also like to thank Dr. Luke Uribarri, Dr. Gautham Ramachandran, and Dr. Ned Allen, all of Lockheed-Martin, for the useful discussions throughout the course of my research. I am grateful for the folks at the CSU CIF, particularly Dr. Pat McCurdy, Dr. Roy Geiss, and Dr. Brian Newell, who all provided excellent training and helped me to develop my skills as scientist.

Several students at The Factory, including Blake Fullenwider, Alex Preston, Trevor Aguirre, Patrick Rodriguez, Mark Bourgeois, Ian Bakst, Anik Faisal, and Brody DeBoer deserve thanks for the assistance and support they have provided during this endeavor. I am also thankful for the rest of the students in my SAMD cohort; I feel that I was very lucky to go through classes with such wonderful people.

I do not have an adequate vocabulary to describe how grateful I am for my Mom and Dad. Their love and support throughout my life made me who I am (for better or for worse). I don't know how they did it, but I think I turned out alright. Finally, I would like to thank my wife, Kathe. I did not know her when I began graduate school, but now I can't imagine my life without her.

TABLE OF CONTENTS

LIST OF TABLES

LIST OF FIGURES

Chapter 1 Introduction

Mayenite electride has emerged as an inexpensive candidate material for thermionic emission devices because of its unique electronic properties and the abundant natural occurrence of its precursor materials. This chapter provides a literature review of previous studies on mayenite and mayenite electride materials, including its structure, functions and relevant processing techniques. In particular, spark plasma sintering (SPS), a field assisted sintering technique that is capable of rapidly consolidating powders to bulk materials, is of interest as a processing method to produce bulk polycrystalline mayenite electride. Current challenges and remaining scientific questions in the field of mayenite electride are addressed in this chapter. In addition, the motivation and objectives of my research are outlined.

1.1 Thermionic Emission

Thermionic emission is defined as a thermally induced flow of charge carriers across a potential barrier. Applications of thermionic emission devices include fluorescent light cathodes, X-ray generation, and beam sources in electron imaging devices. Low work function and thermal stability are desirable properties of thermionic emission materials. The work function of a material is defined as the energy, usually in the form of thermodynamic work, that is required to extract an electron from the material surface into vacuum. A low work function means that a small amount of energy is required to initiate and sustain charge carrier flow from the material surface.[1] This thermionic emission process is demonstrated in Figure 1.1.

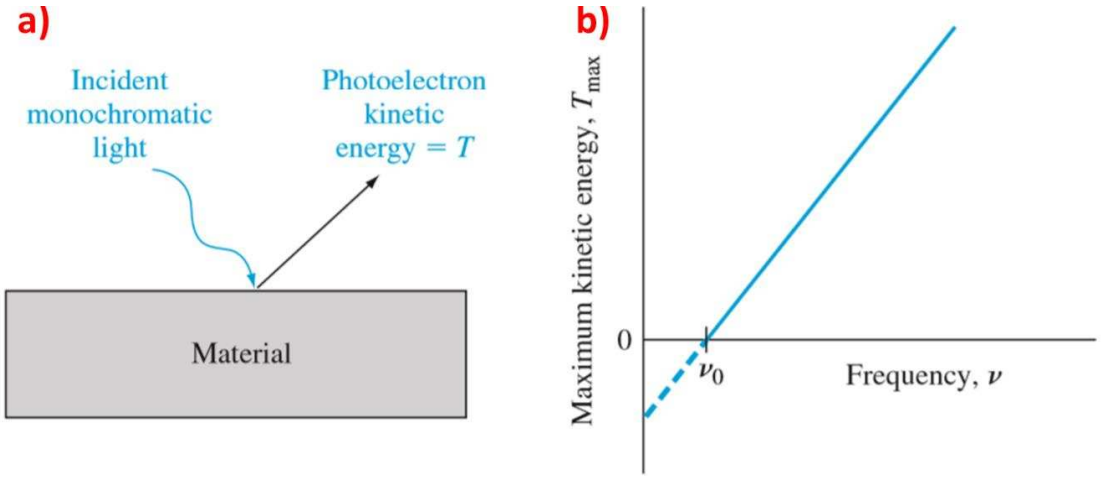

Figure 1.1: Work function as defined by the photoelectric effect a) schematic of physical process b) plot of emitted electron kinetic energy vs. incident light frequency demonstrating a minimum energy required for emission[2]

The work function of a material may most simply be defined as:

$$\Phi = h\nu_0 \qquad \text{Equation 1.1}$$

where Φ is the work function, h is Planck's constant, and ν_0 is the minimal threshold frequency of incident light. While this conceptualization of the work function relates to the photoelectric effect, the thermionic work function is no different. In the case of thermionic emission, energy is applied to the emitting material in the form of heat, rather than incident light.[2]

Thermal stability is controlled by any undesired phase changes or reactions that occur at elevated temperatures that may compromise thermionic emission. Despite W's intermediate work function (4.5 eV), W is commonly used as a thermionic emission filament due to its high melting temperature.[3] CeB_6 and LaB_6 are other common thermionic emission materials because of their low work function values, CeB_6 ~2.59eV and LaB_6 ~ 2.66 eV. LaB_6 is widely used in thermionic emission devices as it has the highest emission slope of the hexaboride family: 29 A/cm^{2}K, meaning that high emission currents may be obtained with small increases of temperature. Despite having a lower emission slope of 15 A/cm^{2}K, CeB_6 is also commonly used as a thermionic

emission source due to its lower evaporation rates at elevated temperatures.[4] Although Ce and La are the most abundant rare earth elements, extracting them from rare earth ores is a lengthy and expensive process. Once the elements are extracted, they must be further processed to form their respective hexaborides.[5]

To reduce the use of rare earth elements, alternative materials are explored in the context of electrides. Electrides are a class of materials which contain clathrated electrons at anionic sites. The high free electron concentration of electrides leads to both low work function and high emission currents. As most electrides decompose above 40°C, their use in thermionic emission devices has been limited.[6] The discovery of a thermally stable electride, mayenite electride, which is comprised of just Ca, Al, and O, has led to a rapid increase in studies of its processing and applications.

1.2 Mayenite and Mayenite Electride

Mayenite is a calcium aluminate phase that has long been known as a secondary phase in Portland cement.[7] The chemical composition of mayenite is $12CaO{\bullet}7Al_2O_3$, which is commonly referred to as C12A7. Determination of the C12A7 crystal structure found that the phase consists of a positively charged Ca-Al-O cage framework, $([Ca_{24}Al_{28}O_{64}]^{4+}$, that contains two O^{2-} anions randomly distributed between six subnano-cages to maintain charge neutrality. Therefore, C12A7 can be also written as $[Ca_{24}Al_{28}O_{64}]^{4+}{:}2O^{2-}$. The unit cell of C12A7 is shown in Figure 1.2a.

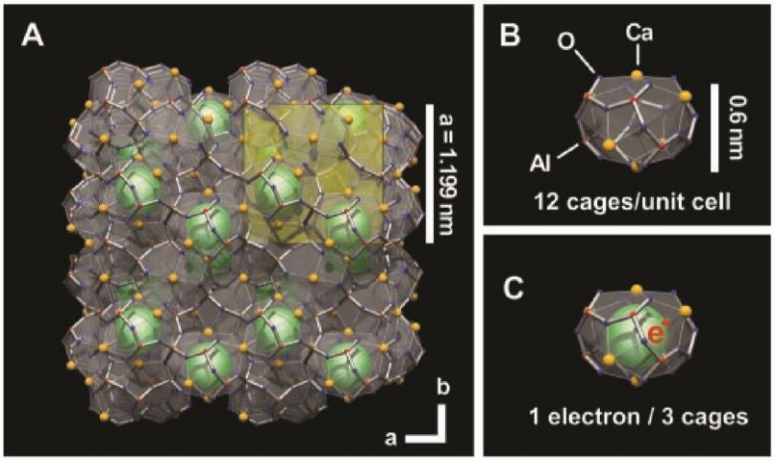

Figure 1.2: Ball and stick representations of C12A7 structural features a) unit cell b) cage containing O^{2-} c) cage containing electron[8]

Research on C12A7 as an O^{2-} emitter showed two types of distinct charge carriers can be emitted: O^{2-} and electrons.[9] It was discovered that if C12A7 was annealed in a reducing environment, O^{2-} is extracted and replaced with electrons to maintain charge neutrality, resulting in the formation of the electride phase, which is thermally stable in air up to 450°C. The reduction reaction is represented by the structural change:

$$[Ca_{24}Al_{28}O_{64}]^{4+}:2O^{2-} \rightarrow [Ca_{24}Al_{28}O_{64}]^{4+}:4e^{-} \qquad \text{Equation 1.2}$$

where e^{-} is an electron. While past modeling work has indicated that the clathrated O^{2-} exists in the cage centers of C12A7, to the best of the author's knowledge, no experimental verification of the location of the delocalized electrons in the electride phase exists. Therefore, the electride phase will be represented as C12A7:e^{-} in this work, with an understanding that this nomenclature simply specifies the electride phase, with no specific claim as to where the excess electrons exist within the electride phase.[10] Assuming every free O^{2-} is replaced by an electron, the theoretical maximum electron density is $2.3 \times 10^{21}/cm^3$.[8] The conversion of C12A7 to C12A7:e^{-} is accompanied by a color change from white to black, as shown in Figure 1.3. This change in the optical behavior of

C12A7:e^- has been attributed to the formation of a cage conduction band (CCB) in the electronic structure, allowing for the absorption of visible light.[11]

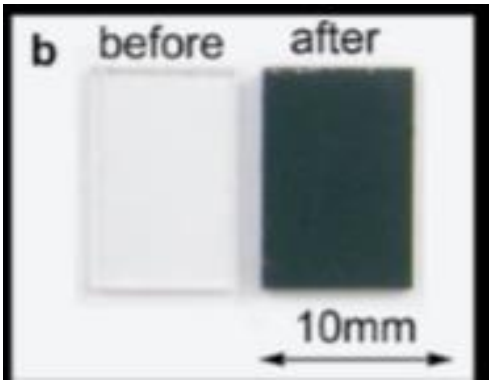

Figure 1.3: Reduction-induced color change leading to black coloration of C12A7:e^-[11]

Several reducing agents have been used to form C12A7:e^-, all to various degrees of success. Metallic Ca was one of the earliest reducing agents. But the formation of an insulative CaO layer on the C12A7 surface prevented continual reduction and ultimately limited the processing temperature. Thus a long-time heat treatment of 240 hours was necessary to form high electron density electride.[8] Ti has taken the place of Ca as a metallic reducing agent as it forms a variety of non-stoichiometric oxides which support O^{2-} diffusion, allowing for continued reduction of C12A7.[12] The work function of these samples was typically around 2.1 eV.[13] C has also been explored as a reducing agent. Reduction by metals occurs by O^{2-} diffusion out of C12A7 and subsequent MO_x formation, whereas reduction by C is accomplished by C diffusing into C12A7, and then reacting with the free O^{2-} to form CO and CO_2, which are subsequently outgassed.[14]

Although it is possible to create C12A7:e^- with near-theoretical maximum electron density to achieve a metallic conduction state, it is difficult to form ohmic contact with the surface of C12A7:e^-, meaning that it yet may behave like an insulator. Conduction through C12A7:e^- is controlled by the ability of electrons to travel through the positively charged cages. As these cages

are atomic-scale structures, it is very difficult to preserve the cages that occur at the free surfaces of C12A7:e^-. These cages may be covered by a non-conductive contaminant layer, or the surface readily absorbs O^{2-} from the air and converts to C12A7, or they may be destroyed by metallographic sample preparation techniques such as cutting or grinding, both of which are common in laboratory and manufacturing settings. Surface cages may be restored by Ar^+ sputtering and subsequent annealing in ultrahigh vacuum conditions.[15] A more time- and cost-efficient method to form a conductive C12A7:e^- sample is to form a percolated composite with conductive particles.

Percolation describes the formation of a conductive network through an insulative matrix. Resistivity/conductivity is difficult to predict for composite materials, but most-difficult for insulator-conductor composites, as microstructural effects dominate the behavior.[16] The microstructural dependence precludes the use of a rule-of-mixtures analysis to determine sample conductivity. A simple schematic diagram is shown in Figure 1.4 to illustrate basic microstructural effects on composite conductivity.

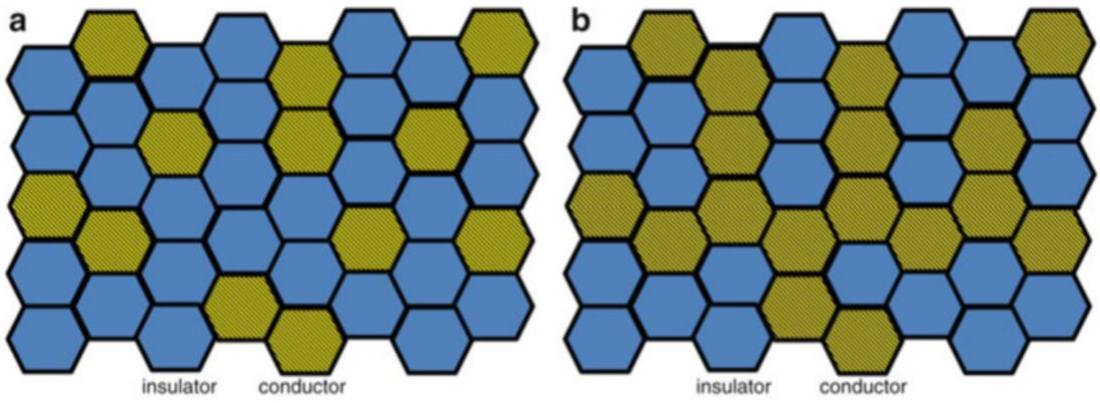

Figure 1.4: Microstructural arrangements of insulator-conductor composites a) insulative composite b) conductive composite showing percolated network[16]

Hayashi successfully created a conductive C12A7:e^--Ti composite by blending C12A7:e^- and Ti powders and consolidating them. While the sample could be machined and directly incorporated into a thermionic emission device, the sample reportedly decomposed above 900°C. No specific description of the decomposition phases was provided.[17] The work also lacked any microstructure characterization.

While the reduction of C12A7 to C12A7:e^- has garnered much attention in the literature, the synthesis of C12A7 powder as a precursor was a prerequisite step in all previous studies, which is a complex and time-consuming process. C12A7 is a stoichiometric compound in the calcium aluminate phase diagram, as seen in Figure 1.5. The CaO-rich phase is tricalcium aluminate (C3A), and the Al_2O_3-rich phase is monocalcium aluminate (CA). Both phases are electrically insulative, and as such it is desired to minimize their occurrence in bulk C12A7. Precursor C12A7 is commonly grown as a single crystal via the floating zone method (FZM), deposited as a thin film via pulsed laser deposition (PLD), or produced as a polycrystalline powder through a myriad of chemical reactions.[18–20] As this study is focused on processing C12A7:e^- through powder metallurgy techniques, the following discussion will focus on the formation of polycrystalline powders.

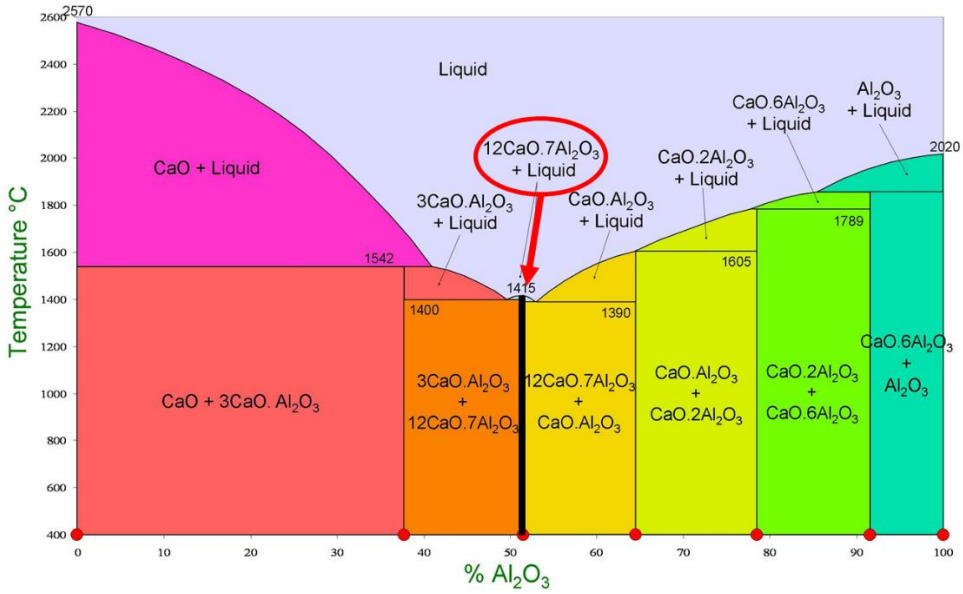

Figure 1.5: Calcium aluminate phase diagram showing C12A7 as a stoichiometric compound[21]

C12A7 powders are primarily produced through two processes: sol-gel methods and solid-state reactions (SSR). Sol-gel methods involve the use of nitrates or chlorides of Ca and Al and a chelating agent, typically citric acid.[22] When the precursors are mixed together such that stoichiometry between the metals is obtained, the chelating agent can be used to stabilize the metal cations and allow for the formation of C12A7 during subsequent heat-treatment. SSR formation of C12A7 is accomplished by blending $CaCO_3$ and Al_2O_3 in a 12:7 stoichiometric molar ratio and heat-treating the powder blend for approximately ten hours between 1200°C and 1400°C. It has been shown that the microstructure of calcium aluminates formed during SSR processing is onion-like, with Al_2O_3 in the center and increasingly CaO-rich phases forming the outer layers (Fig. 1.6).[23]

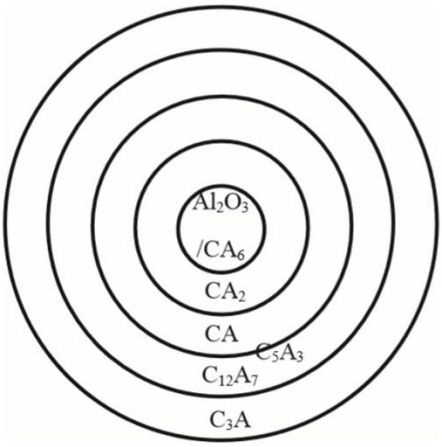

Figure 1.6: Schematic of calcium aluminate phase formation showing an increase in Al_2O_3 towards the center of the particle[23]

A detailed comparison between these methods has been performed elsewhere.[24] It was determined that the high chemical homogeneity provided by the sol-gel method allowed for C12A7 formation at lower temperatures (1100-1200°C) since relatively short diffusional distances were required.[22,25] Despite the lower processing temperatures required, sol-gel methods typically require longer processing times, sometimes up to 48 hours, as well as additional precursor chemicals.[24] Yields are also limited by size of processing equipment. The use of powder processes like SSR treatment allows for the facile production of percolated composites with a variety of compositing materials.

Precursors for SSR processing are typically mixed together via ball milling. Ball milling is a solid-state powder processing method where powders are subjected to repeated impacts from the collisions between the milling media (ball-to-ball and ball-to-wall collisions). Planetary ball milling (PBM) involves the rotation of multiple jars around a central axis coupled with the counter-rotation of each jar around their axis. The rapid change in centrifugal forces lead to a combination of grinding and impacting, which affects both particle size and morphology. PBM is common in research settings due to the relative size of equipment and high degree of control over process

parameters.[26] Yields of over hundreds of grams per batch can be achieved. There are several important processing parameters in PBM, including the chemical composition of jars and media, ball to powder weight ratio, media size, RPM, milling time, and duty cycle. PBM has been used to form C12A7 SSR precursors in several studies.[27–29] However, details of milling parameters are sparsely reported, and no specific investigation into the effect of milling parameters on C12A7 formation has been performed, despite of a study suggesting that calcium aluminate formation may be facilitated by mechanical activation.[30]

Eufinger produced pure C12A7 phase by hand-mixing precursor powders and heat-treating the powders at 1400°C for 16 hours, followed by additional grinding and repeating the heat-treatment.[27] Zou produced insulative C12A7 by ball milling precursor powders with agate media for four hours with a milling speed of 300 RPM. Ball to powder weigh ratio and ball diameter are not reported. SSR processing was performed at 1250°C for eight hours.[28] Rudradawong reported that $CaCO_3$ and Al_2O_3 powders were mixed in a 12:7 stoichiometric ratio for 24 hours, and then subjected to SSR processing at 1250°C for five hours.[29] No report of jar/media composition or other milling parameters other than time are included, but one may observe that longer milling time allowed for successful SSR processing at lower temperature and shorter time.

Bulk C12A7 materials are commonly made via sintering of C12A7 powder. Sintering and densification occur when a heat-treatment is performed to densify a powder compact. Free sintering involves firing a green-pressed powder compact at elevated temperatures for extended times, in the absence of any additional forces. The sintering process typically consists of three stages. The first stage of sintering involves the formation of necks between particles via evaporation-condensation and surface diffusion (Fig. 1.7b). This stage results in minimal densification, as the centers of mass for each particle do not move closer to each other. Once

sufficient necking areas have formed, the second stage of sintering initiates. In this stage, mass transports from the interior of the particles via grain-boundary diffusion, volume diffusion, and plastic flow. Significant densification occurs during this stage (Fig 1.7c). In the final stage of sintering, pores close and grain-growth initiates. Minimal densification occurs during this stage (Fig 1.7d).[31]

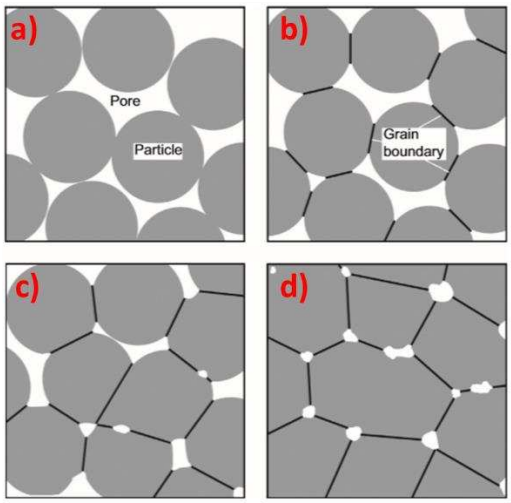

Figure 1.7: Schematic of sintering process a) loose powder b) first stage c) second stage d) third stage of sintering. Adapted from German[31]

While the reduction of interfacial energy is the primary driving force in sintering, there are several pathways to modify the process. External forces, such as mechanical pressure or an electric field may be applied to accelerate densification. Pressure may be applied uniaxially or isostatically, leading to a stress amplification at pores that motivates mass transport. An applied electric field affects the formation and densification of ionic materials, including C12A7 and other calcium aluminate phases, by increasing the mobility of the ions.[32] Powder modifications may also have significant effects on the densification of powder compacts. The formation of reaction layers on particle surfaces or liquid phases may facilitate the densification of refractory materials. Similarly, diffusion in chemically heterogeneous systems or the procession of a chemical reaction may

dominate mass-transport behavior, leading to reactive sintering.[33] Reactive sintering has successfully been applied to the formation of porous C12A7 bodies.[34] Common sintering of C12A7 or C12A7:e^- takes a time length of several hours. In the research reported herein we applied a field assisted sintering technique, named spark plasma sintering, to reduce the processing time of making bulk C12A7 based materials.

1.3 Spark Plasma Sintering

Spark plasma sintering (SPS) is a powder consolidation technique where high heating rates are achieved by passing high currents through graphite tooling. Graphite is commonly used as the tooling material due to its high conductivity and compressive strength at elevated temperatures. The SPS system used in this work is shown in Figure 1.8.

Figure 1.8: Picture of Fuji MK 3.2 SPS system[35]

SPS is typically performed under vacuum or in the presence of an inert gas to prevent the degradation of the graphite tooling at elevated temperatures. Uniaxial pressure is applied

throughout the SPS process to ensure proper current flow though the graphite tooling, as well as to aid densification. Applied pressure facilitates densification by establishing larger contact areas between particles and enhances densifying mass transport mechanisms. SPS is also advantageous over traditional sintering as the rapid heating rates allow for faster activation of densification. Grain-boundary and volume diffusion typically have higher activation energies than surface diffusion, which implies that one must first initiate non-densifying mass transport before densification can begin. However, the high heating rates in SPS allow for non-densifying mass transport mechanisms to be bypassed or minimized.[36] The reducing environment created during the SPS process, as well as the rapid processing times, have made it a promising means of consolidation of C12A7, as well as the formation of C12A7:e^-.

Chung was the first to show that reduction of C12A7 to C12A7:e^- could occur in SPS due to the diffusion of C_2^{2-} anions from the graphite tooling into C12A7. 1g of C12A7 powder was sintered at 1100°C for ten minutes with a heating rate of 100°C/min and an applied pressure of 40 MPa. The SPS chamber pressure was reported as 10^{-5} Pa. The reduction of C12A7 by the diffusion of C_2^{2-} was verified by the presence of C_2^{2-} in Raman spectroscopy scans of C12A7 samples sintered at lower temperatures.[37] Color change of C12A7 samples with respect to increasing sintering temperature is shown in Figure 1.9. The maximum electron concentration achieved by this method was 5.3 x $10^{19}/cm^3$.

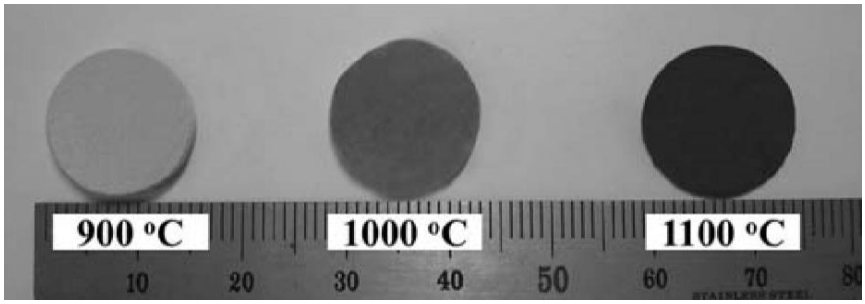

Figure 1.9: Color change of C12A7 consolidated via SPS at various temperatures[37]

Li et al. demonstrated that C12A7 could also be reduced to C12A7:e^- in SPS by placing Ti powder above and below C12A7 such that Ti_3O formed in both layers. Samples were sintered at 1150°C for 20 minutes with a heating rate of 120°C/min and an applied pressure of 40 MPa. SPS chamber was reported as 10^{-3} Pa. Sample mass was not reported. A similar variation of sample color with respect to temperature was reported. It is interesting to note that reduction of C12A7 by Ti in this configuration did not lead to the decomposition of C12A7, but attempts to composite C12A7 with Ti particles led to a reported decomposition above 900°C.[17,38] The thermionic emission properties of this sample were measured. A maximum emission current of 1.68 A/cm^2 was achieved at 1100°C and an accelerating voltage of 35 kV/cm. The work function was evaluated as 2.13 eV.

Reactive sintering of C12A7:e^- in SPS was recently achieved. C12A7+C3A precursor powders were prepared vis SSR processing. This powder mixture was then annealed at 1000°C for 20 hours in an evacuated quartz tube at 10^{-5} Pa. After this treatment, the powder was ball milled with Al powder with cemented carbide media in an Ar environment. After this treatment, the C12A7+C3A+Al mixture was sintered via SPS at 1050°C for five minutes with a heating rate of 50°C/min and an applied pressure of 60 MPa. Reported SPS chamber pressure was 10^{-4} Pa. No secondary phases were reported after the process. Here, Al acted as the reducing agent for the

conversion of C12A7 to C12A7:e^-, resulting in the formation of Al_2O_3. Al_2O_3 then reacted with C3A to complete the formation of C12A7:e^-.[39]

1.4 Motivation and Objectives

The literature review above showed that fundamental knowledge of the structure and functionality of C12A7:e^- is advancing in the field, and a variety of synthesis routes have been developed to make bulk C12A7:e^-. However, several challenges and knowledge gaps still exist in the field. First, the formation of other calcium aluminate phases during the synthesis of C12A7 or C12A7:e^- has been overlooked. Second, most of the previous studies also lack detailed microstructure characterization. In addition, monolithic C12A7:e^- does not provide continuous ohmic contact due to the destruction of the surface cages during processing, which limits its direct use in thermionic emission devices. The use of particulate Ti to form a percolating network has allowed for C12A7:e^- to be used in thermionic emission circuits without the use of additional metallic coatings. But adding Ti led to the decomposition of C12A7:e^- above 900°C. Dense C12A7 may be rapidly produced via SPS, and the reducing environment associated with SPS can lead to the concurrent consolidation and reduction of C12A7 powder to dense C12A7:e^-, via carbothermal reduction. Ti foil has successfully been used in SPS to achieve rapid reduction of C12A7 with no observed decomposition, whereas the use of Ti powder interspersed with C12A7 in SPS led to decomposition of C12A7.

While there has been much progress in understanding the processing of C12A7 and C12A7:e^-, the current knowledge of C12A7-based materials lacks fundamental understanding of the effect of adding secondary phase/particles on the formation of C12A7:e^-. It is known now that decomposition of C12A7:e^- occurs when Ti is added to make C12A7:e^- composite materials.

However, the mode of decomposition is unclear and reaction phases are unknown. Were this information available, it may be useful for the design of other C12A7:e^- composites. Beyond the interactions between C12A7:e^- and Ti, no other additives have been investigated for the formation of a percolated C12A7:e^- composite. SPS processing has become attractive for the consolidation of C12A7 due to the fast processing rates. While SPS processing has greatly reduced consolidation and reduction time, synthesis of C12A7 powder as feedstock for SPS is still a time-consuming process.

To address the aforementioned practical issues and to fill in the fundamental knowledge gap, this research investigated the effect of adding different reinforcing particles, including carbon black (CB), Ti, and TiB_2, on the formation of C12A7:e^- via spark plasma sintering (SPS), with attention particularly paid to address phase formation during the processing. This work will investigate any secondary phases formed and their potential effect on the functionality of the composite for thermionic emission purposes. Specifically, preformed C12A7 powder was synthesized via a solid-state reaction and used as the precursor base in SPS to study the effect of additives. In addition, a novel approach using *in-situ* reaction in SPS was proposed in the present work to significantly reduce the processing time.

Experimental approaches will be described in CH. 2, including the procedures for creating C12A7 powder, subsequent compositing and consolidation, microstructure characterization of samples, and electronic property testing. Results of C12A7:e^- composite materials made from preformed C12A7 powder will be discussed in CH. 3 to reveal the effects of adding conductive phases for percolation, including Ti, TiB_2, and CB, with a comparison to monolithic C12A7 and C12A7:e^-. An investigation into the *in-situ* formation of C12A7 from reaction sintering of $CaCO_3$ and Al_2O_3 is described in CH. 4. The production of C12A7:e^- composites with complex geometries

will be discussed in CH. 5, as well as the application of different electronic characterization methods. Finally, a summary of this work will be discussed, and future work will be proposed in CH. 6.

Chapter 2 Approach: Experimental Procedure and Characterization Methods

This chapter will describe the experimental procedure and characterization methods used in my research. Formation of mayenite (C12A7) powder was achieved by ball milling and heat-treating precursor powders. C12A7 powder was subsequently blended with carbon black (CB), Ti, and TiB_2, and consolidated via spark plasma sintering (SPS). Preformed C12A7 was also consolidated with Ti-foil above and below the powder in SPS. The *in-situ* formation of mayenite electride (C12A7:e^-) is attempted, and the importance of different process parameters is identified. The microstructures of C12A7 and C12A7:e^- consolidated with various additives via spark plasma sintering (SPS) are investigated via scanning electron microscopy (SEM) and energy-dispersive X-ray spectroscopy (EDS). Crystal structures are evaluated by X-ray diffraction (XRD). Thermogravimetric analysis and differential thermal analysis (TG/DTA) are used to study the onset temperatures of the various reactions involved in solid state reaction (SSR) processing of calcium aluminates. The electronic properties of select C12A7:e^- samples are characterized by Kelvin probe force microscopy (KPFM), thermionic emission testing, and electron paramagnetic resonance (EPR). C12A7:e^- composite samples with complex geometries are manufactured to allow for thermionic emission characterization. Rationale for material and process selection is also discussed in this chapter.

2.1 Overview of the approach

The work presented here follows two distinct paths, the first being the consolidation of preformed C12A7 with various additives, and the second being the *in-situ* formation of C12A7 during SPS processing. The study of preformed C12A7 will be discussed in CH. 3, while *in-situ*

processing attempts will be discussed in CH. 4. The electronic properties of samples processed via both routes are characterized and discussed in CH. 5. The experimental approach overview is provided schematically in Figure 2.1.

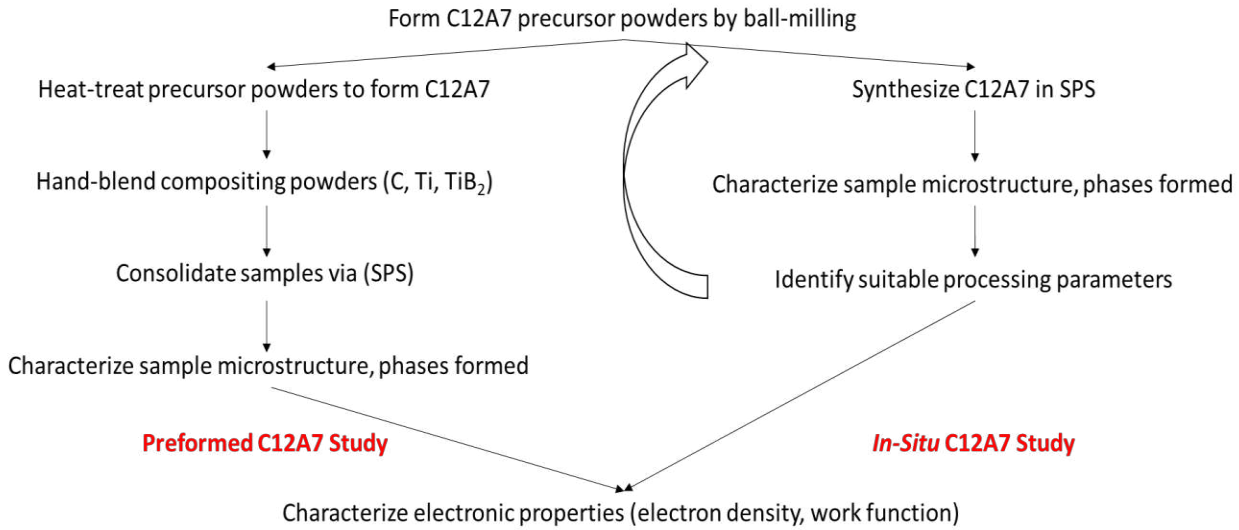

Figure 2.1: Process flowchart describing the two primary branches of this work

2.2 Process and Material Selection

Formation of C12A7 powder is performed by mixing $CaCO_3$ ($CaCO_3$ anhydrous, VWR) and Al_2O_3 (α-Al_2O_3 <1.0 μm, Alfa Aesar) powders and reacting the mixture in air at 1300°C, which is below the melting point of C12A7 (1415°C).[40] This SSR approach to form C12A7 is selected over sol-gel methods due to its facile nature. $CaCO_3$ and Al_2O_3 powders are blended via planetary ball milling using an Across International PQ-N4 planetary ball mill (Fig. 2.2). Low-energy mixing methods such as hand mixing or using a stir rod were attempted, but these did not provide sufficient mixing, i.e. secondary calcium aluminate phases are formed after SSR processing. Ball milling is performed using Al_2O_3 jars and media. Al_2O_3 jars and media are selected as they minimize powder contamination. While there are several parameters that must be controlled during ball milling, this

work will only investigate the effect of milling time on calcium aluminate formation during SSR processing.

Figure 2.2: Across International PQ-N4 Planetary Ball Mill[41]

$CaCO_3$ and Al_2O_3 are milled at 400 RPM using a five minutes on/ten minutes off duty cycle to minimize frictional heating in the jars. A ball:powder weight ratio of 10:1 is used throughout the study, with 40wt% of the balls consisting of 6mm diameter balls, and the remainder consisting of 10mm diameter balls.

SPS is selected to consolidate the C12A7 powders. SPS is selected as it allows for reduced processing times, being able to produce a dense 18mm-diameter by 5mm-thick puck in under ten minutes. A schematic of a typical SPS machine is shown in Figure 2.3 The atmospheric conditions required by SPS also promote the conversion of C12A7 to C12A7:e^-. SPS is typically performed in low O_2 environments to prevent degradation of the graphite tooling. While SPS is typically performed in vacuum, inert gases such as nitrogen or argon may be used. As one of the goals of this study was to convert C12A7 to C12A7:e^- during consolidation, experiments are performed in vacuum to minimize the O_2 partial pressure. A base pressure of 10 Pa is established in the sintering

chamber and is monitored throughout the experiment by a Pirani gauge. It has been shown that the speed at which C12A7 is converted to C12A7:e^- is directly related to the O_2 partial pressure during sintering. In other SPS studies of C12A7, chamber pressures on the order of 10^{-3} Pa are observed, which is several orders of magnitude lower than the pressure achieved in this study.[38] To account for this, higher sintering temperatures are used to allow for reduction in a similar time scale.

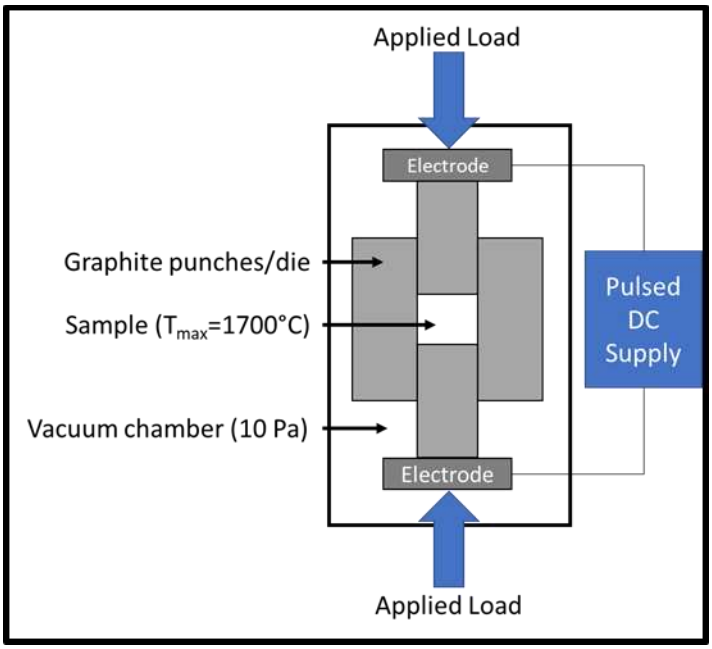

Figure 2.3: Schematic of SPS machine

Sintering temperatures are typically explained in terms of the homologous temperature, T_H, which is a ratio of the absolute sintering temperature to the absolute melting temperature of the material being sintered. Traditional sintering procedures use homologous temperatures between T_H=0.5-0.8. A homologous temperature of 0.87 (1200°C) is used in this study as this high temperature provides fast reduction of C12A7 to C12A7:e^-. Sample temperature is measured by an IR-pyrometer mounted to the exterior of the sintering chamber. The IR pyrometer is selected over a K-type thermocouple due to its superior performance at temperatures at and above 1200°C.

A ten-minute hold time is used throughout this study. This hold allows for continued reduction of C12A7 to C12A7:e^-.

$CaCO_3$ is selected as C12A7 precursor over CaO as CaO is both caustic and hygroscopic, making safe storage and handling a non-trivial endeavor. Ti (-325 mesh, 99.5% metal basis, Alfa Aesar) is selected as a compositing material as it has been shown in literature to effectively reduce C12A7 to C12A7:e^-, as well as to form an effective percolating network below 900°C.[17] CB (Carbon Black 99%+C Powder, Global Graphene Technologies) is also selected as a compositing material as C will also reduce C12A7.[22] C12A7-C composites have not been explored in literature, however as C in the graphitic phase has a high electrical conductivity, it is hypothesized that C will provide this functionality. TiB_2 (-325 mesh powder, Alfa Aesar) is the final selected compositing material. TiB_2 has not been shown to reduce C12A7. Due to TiB_2's high conductivity, as well as its high O-affinity, it is reasonable to hypothesize that TiB_2 will provide the desired effects.[42]

2.3 Preformed Mayenite Study

To form C12A7 powder, $CaCO_3$ and Al_2O_3 were ball milled together in a 12:7 stoichiometric ratio for ten minutes, using the milling parameters described above. These precursor powders were heat-treated at 1300°C for ten hours. C12A7 formation was verified via XRD. C12A7 was then ground into a powder using an agate mortar and pestle. C12A7 powder was then consolidated using the SPS parameters described above. Table 2.1 shows a list of sample IDs as well as the additives in each sample.

Table 2.1: Sample identifications (IDs) and additives

Sample ID	Additives
C12A7-P	100 wt% C12A7
C12A7-Foil	100 wt% C12A7 between 2 Ti foil sheets
C12A7-C	90 wt% C12A7, 10 wt% CB
C12A7-Ti	50 wt% C12A7, 50 wt% Ti
C12A7-TiB_2	70wt% C12A7, 30 wt% TiB_2

The density of each sample was determined via Archimedes' method using DI water as the medium. The density of sample was recorded to verify that samples contained minimal porosity. The conductivity of each sample was evaluated using a multimeter. This facile test indicated whether percolation had been achieved in each composite sample, or if mobile electrons were present in C12A7. Samples were cross sectioned using a 5" x 0.015" x 1/2" Medium grit, high conc. DIAMAT Wafering Blade mounted in a PICO 155 saw (Pace Technologies). Samples were polished, with a final step of 0.05μm diamond abrasive. Optical images were taken using a Zeiss Stemi 508 stereomicroscope.

The crystal structures present in each sample were characterized via XRD using a Bruker D8 Discover DaVinci Powder X-ray Diffractometer. Scans were collected between 28°-50° 2θ, using Cu kα radiation. Sample microstructures were characterized using a JEOL JSM-6500 FE SEM with an acceleration voltage of 15kV in conjunction with an Oxford Instruments Max 80 SSD EDS detector, using a pulse processing time of 6 to achieve a dead time below 35%. Scale bars were added to optical and SEM images using ImageJ.

2.4 *In-Situ* Mayenite Study

To initiate this portion of the study, the ball milled precursor powders described in Section 2.3 were used as the feedstock in SPS and sintered directly. As it was discovered that ten minutes

of ball milling did not mix the precursors well enough to form C12A7 in the desired time frame, longer milling times were explored. Precursor powders were ball milled for two and ten hours. All sets of precursor powders were characterized by XRD to observe if milling time had any effect on peak intensities or locations. Powders were also characterized by TG/DTA to determine if ball milling time had any effect on the calcium aluminate formation reaction.TG/DTA (SEIKO) is performed using Pt pans in flowing Ar (200mL/min) using a heating rate of 5°C/min to observe if there is any change in the reaction behavior with respect to milling time. Scans were performed between 50°C and 1100°C. Powders post TG/DTA were also characterized by XRD to observe if milling time had any effect on the rate of calcium aluminate phase formation.

The effect of heating rate on calcium aluminate formation in SPS was also investigated. Precursor powders were characterized by TG/DTA using heating rates of 5, 10, 20, and 50°C/min and otherwise identical parameters to those described above to determine if high heating rates, such as those used in SPS (100°C/min), could affect calcium aluminate phase formation. To complete this portion of the investigation, an *in-situ* reaction was performed in SPS using a heating rate of 5°C/min in the temperature range of interest.

The effect of different additives on the *in-situ* formation of C12A7 in SPS was also explored. Ti and CB were blended with the ball milled precursor powders using the same wt%s from Section 2.3 and sintered. The microstructure and phases formed were characterized by SEM/EDS and XRD.

2.5 Samples with Complex Geometries

C12A7:e^- composite samples shaped like hemispheres with stems on the flat face were produced via SPS processing for thermionic emission characterization. C12A7:e^--Ti and C12A7:e^--TiB_2 composite hemispheres were sintered using the wt%s of each additive as described in Section

2.3. The diffusion of C into C12A7:e^- from the surrounding graphite tooling made sample removal challenging, as the tooling would essentially bond to the hemisphere. To extract each sample without fracture, notches were cut into the lower hemisphere punch. The lower punch was then mounted in a vise, and material was broken away using a hammer and punch. Once the lower hemisphere punch was removed, the upper punch was removed by using the slow speed saw. The stems were exposed by adhering 180-grit SiC abrasive paper (Pace Technologies) to the face of a razor blade and carefully grinding away the remaining graphite.

In addition to sintering samples with the hemisphere-stem geometry, these samples required post-processing such that they could be affixed to a thermionic emission testing apparatus by a threaded rod. To add the threaded hole to the C12A7:e^--Ti hemispheres, Ti tubes were sintered via SPS using the tooling shown schematically in Figure 2.4. A graphite rod was centered between the SPS punches to form the ID of the Ti tubes. Ti tubes were consolidated using a heating rate of 100°C/min from room temperature to 1100°C with an isothermal hold of one minute. A uniaxial pressure of 30 MPa was applied throughout sintering. After consolidation, the graphite rod was drilled out of the Ti tube and was subsequently hand-tapped for the desired thread geometry. 5mm slices were cut from these tubes and faces were polished to a defect size of 0.05μm. These slices were then placed on the flat face of the composite hemispheres, and diffusion bonded via SPS. A heating rate of 100°C/min from room temperature to 700°C and an isothermal hold time of five minutes was used to bond the Ti backing piece. Minimal SPS applied load (2.5 kN) was applied to minimize plastic deformation and preserve the geometries of the hemisphere and the threaded hole. After bonding, the hole was re-tapped to verify that the hemisphere could be successfully mounted.

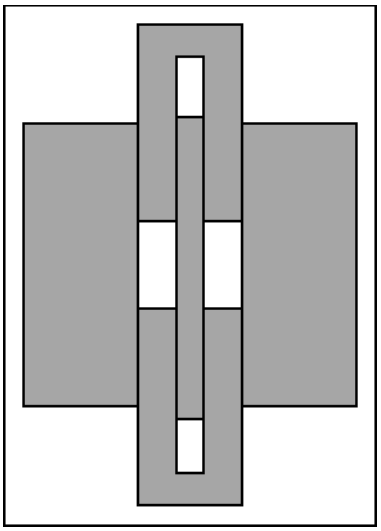

Figure 2.4: Schematic of SPS tooling used to sinter Ti tubes

This method could not be applied to the TiB_2-composite hemispheres as TiB_2 does not readily bond to Ti. To insert the threaded rods into the TiB_2-composite hemispheres, 4mm, 6mm, and 8mm diamond-coated wet cut drill bits were used to remove material from the back of the hemispheres. Hemispheres were mounted in a lathe using a custom sample holder and drilled using 400 RPM and a feed rate of 0.25mm/min. Water was continuously sprayed onto the cutting tools to keep them cool as well as facilitate the removal of material. Graphite rods were press-fit into the remaining holes and ground flush with the stem. These rods were then drilled and tapped. These processes will be described in more detail in CH. 5.

2.6 Electronic Characterization

Three electronic characterization techniques were used in this study: Kelvin probe force microscopy (KPFM), thermionic emission testing, and electron paramagnetic resonance (EPR). KPFM is an atomic force microscopy (AFM)-based approach for determining the work function of a material with high spatial resolution, on the order of nanometers.[43] This technique is particularly useful for characterizing local work function variation in composite materials.

Thermionic emission testing is a method for directly measuring the emission current of a material with respect to temperature and applied voltage. In addition to measuring emission currents, the work function of a material may be extracted. Thermionic emission testing was performed in vacuum at 1200°C. EPR characterizes the behavior of unpaired charge carriers in a material by measuring changes in microwave absorption with respect to a changing magnetic field. Samples for KPFM and thermionic emission testing were cut from an *in-situ* sintered C12A7:e^--Ti composite. Samples for EPR were taken from C12A7-C and C12A7-Foil. EPR was performed using X-band microwaves (9.8GHz) and fused quartz sample holders to minimize background signal. Samples with dimensions of 2mm by 2mm by 1mm were cut for KPFM and thermionic emission testing. Samples were polished, with a final step using 0.05μm diamond abrasive. Samples with dimensions of 1mm by 1mm by 6mm were cut for EPR testing.

Chapter 3 Mayenite Electride Composite Materials Using Preformed Mayenite Powder

This chapter aims to investigate the effects of addition of different reinforcing phases on the phase formation and microstructure in the mayenite (C12A7) or mayenite electride (C12A7:e^-) composite materials that were made from preformed C12A7 powders. Three different reinforcing phases were studied: carbon black (CB), Ti, and TiB_2. Results suggest that the Ti-foil method provided the most efficient reduction of C12A7 to C12A7:e^- without decomposition of C12A7 to any secondary calcium aluminate phases. In contrast, samples reinforced with Ti or TiB_2 exhibited secondary calcium aluminate phases such as C3A in the case of Ti and CA in the case of TiB_2.

3.1 Preformed Powder Characterization

Figure 3.1 shows a picture of the preformed C12A7 powder, as well as the XRD pattern of the powder. The powder is white, indicating that it is insulative C12A7 (Fig. 3.1a).[8] Virtually no secondary calcium aluminate phases are seen in the XRD pattern, which indicates that any secondary calcium aluminate phases observed after SPS processing is due to decomposition during SPS.

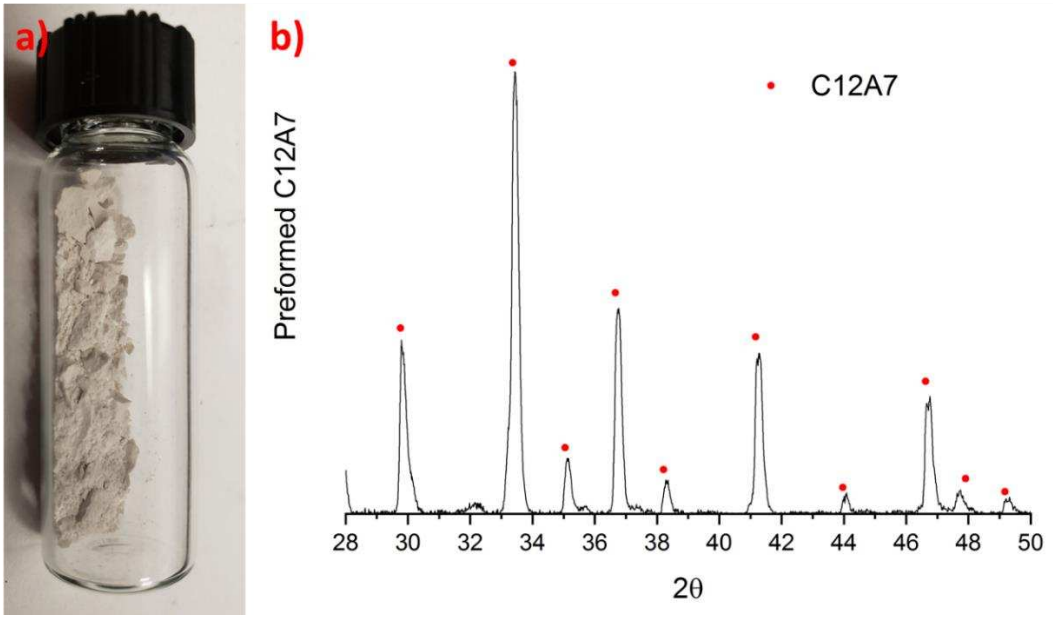

Figure 3.1: Overview of preformed C12A7 powder a) representative sample of powder showing white color b) XRD pattern showing formation of C12A7

3.2 Density and Conductivity

The identifications of various samples, as well as the corresponding density and conductivity, are provided in Table 3.1. Archimedes measurements suggest that all the samples are over 95% dense. Figure 3.2 shows the pictures of the as-sintered samples and the cross-section microstructure images from optical microscopy. C12A7-P (Fig. 3.2a) exhibited a white color, indicating the formation of insulative C12A7.[8] In contrast, C12A7-Foil (Fig. 3.2c) and C12A7-Ti (Fig. 3.2d) exhibit predominately a black or dark green color, indicating the formation of C12A7:e^-. C12A7-C (Fig. 3.2b) contains both regions of light color and regions of dark color, as well as several large grains exhibiting an intermediate color, indicating that some C12A7:e^- formed, but the reduction of C12A7 to the electride phase was not uniform. C12A7-TiB_2 (Fig. 3.2e) contains several black and dark gray regions, indicating the formation of C12A7:e^-. The difference in

sample color from optical microscopy also suggests that the amount of the electride phase in C12A7-TiB_2 may lie between that of C12A7-C and that of C12A7-Ti.

Table 3.1: Sample IDs, additives, and densities via Archimedes

Sample ID	Additives	Relative Density (%)	Conductivity (S/cm)
C12A7-P	100 wt% C12A7	95	N/A
C12A7-Foil	100 wt% C12A7 between 2 Ti foil sheets	98	1.14
C12A7-C	90 wt% C12A7, 10 wt% carbon black	99	0.28
C12A7-Ti	50 wt% C12A7, 50 wt% Ti	99	1.72
C12A7-TiB_2	70wt% C12A7, 30 wt% TiB_2	98	0.40

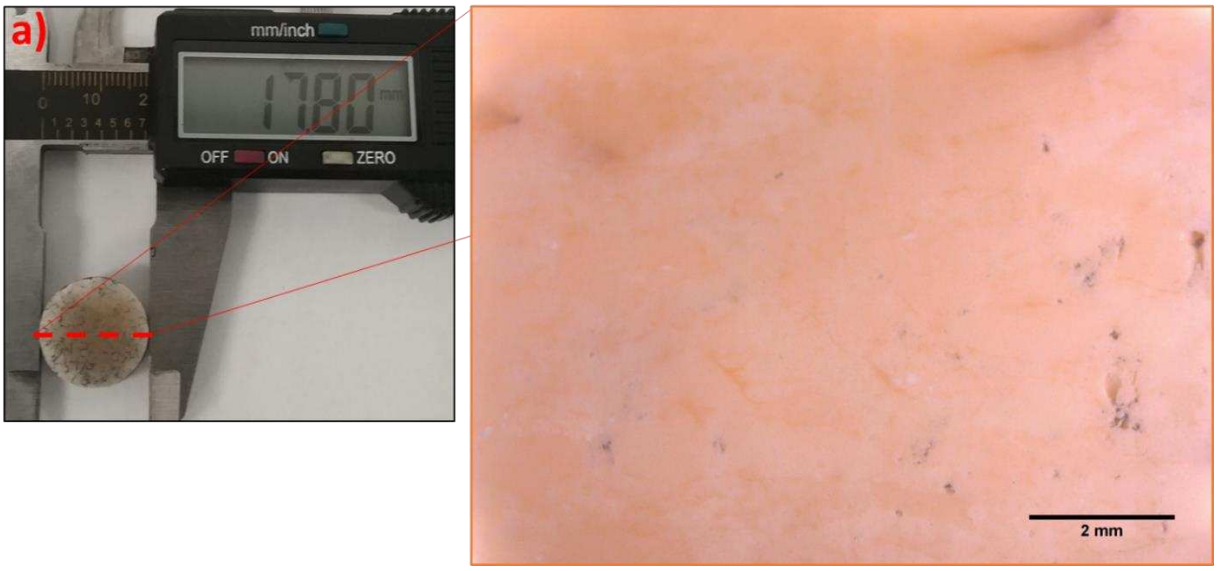

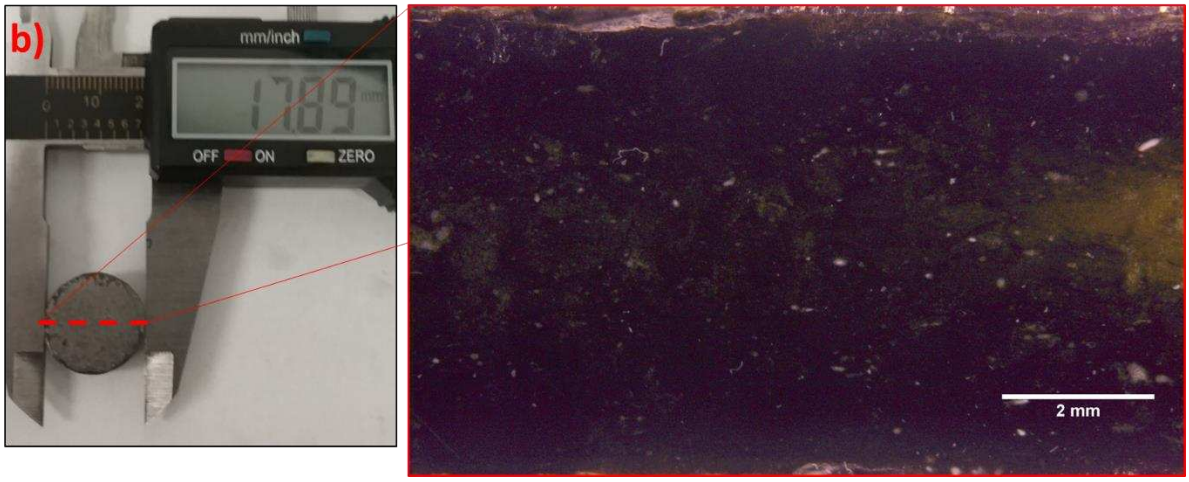
b)
mm/inch
17.89
OFF ON ZERO
2 mm

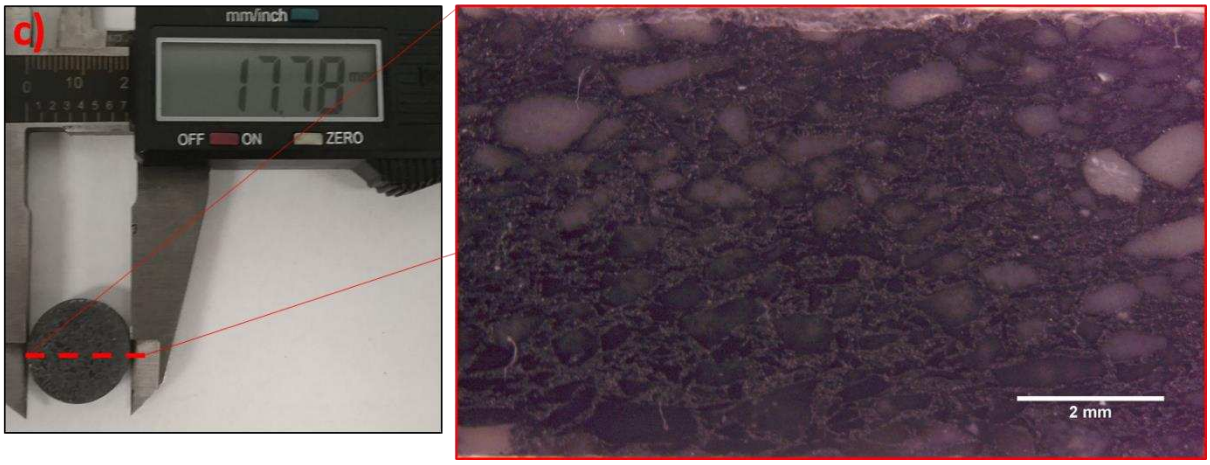
c)
mm/inch
17.78
OFF ON ZERO
2 mm

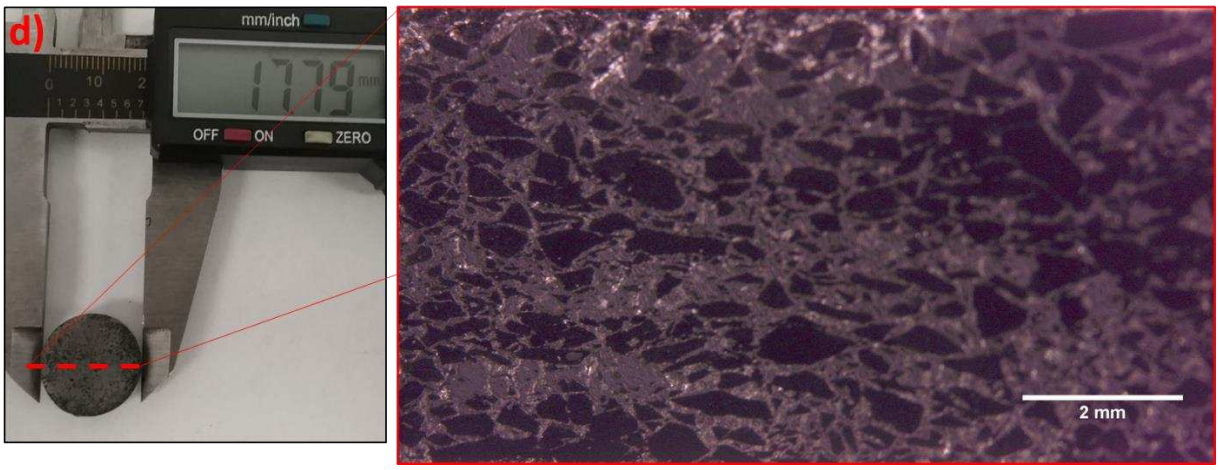
d)
mm/inch
17.79
OFF ON ZERO
2 mm

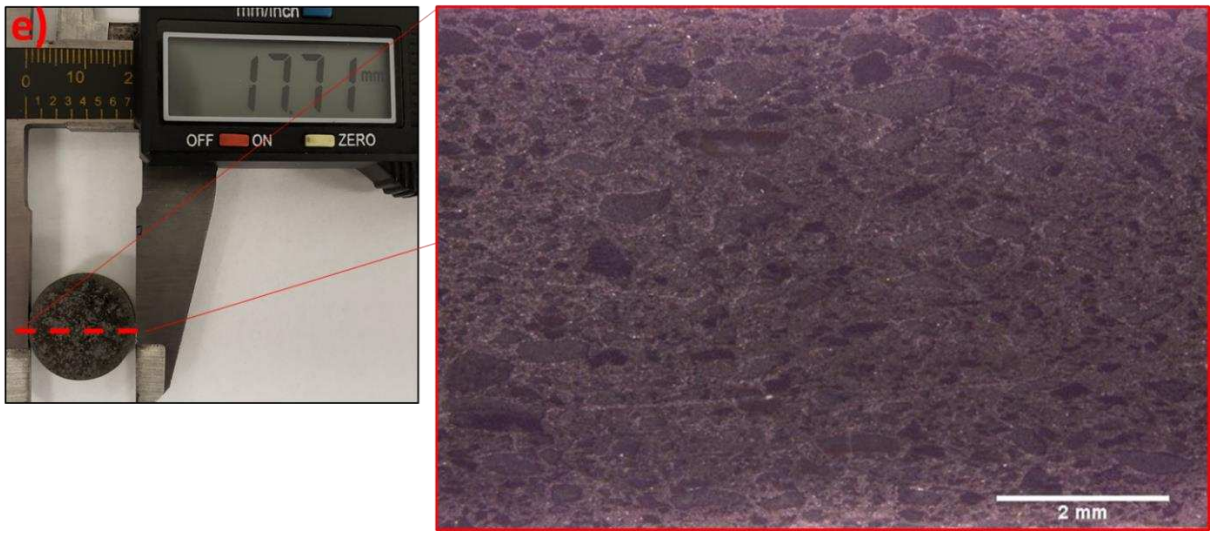

Figure 3.2: Pictures of the as-sintered samples and the optical images of their cross-sections: a) C12A7-P b) C12A7-Foil c) C12A7-C d) C12A7-Ti e) C12A7-TiB_2

All composite samples display ohmic contact, indicating that the reinforcing phases form a continuous network in the composite. The conductivity of C12A7-Ti is higher than those of C12A7-C and C12A7-TiB_2. The conductivity of insulator-conductor composites is dominated by the microstructure, particularly the phase connectivity.[44] Previous modeling work, based on an assumption that all particles are spherical and have an identical size, and the distribution of phases is random, identified that the critical volume fraction of the conductive phase is approximately 30 vol%. The contacts between the conductive phases can develop a chain or network that span through the composite when the conductive phase exceeds 30 vol%. In contrast, below 30 vol% the conductive phases become isolated from each other, leading to a drop in the conductivity by several orders of magnitude.[16] In the current study, The volume fraction of the conductive reinforcing phase for the C12A7-C, C12A7-TiB_2, and C12A7-Ti composites are 12 vol% CB, 20 vol% TiB_2, and 37 vol% Ti, respectively. The higher conductivity of the C12A7-Ti composite is attributed to the higher volume fraction of the conductive reinforcing phase, i.e., Ti. The composite samples were all polished to remove graphite from their faces prior to measuring conductivity,

which would have destroyed the surface cages of C12A7:e^-. Therefore, in these samples any conductivity at the surface must be attributed to the reinforcing phase. Pristine C12A7:e^- in the sample interiors does influence the bulk conductivity, but the estimation of its effects is beyond the scope of this work.

In contrast, mechanical removal of the graphite foil from C12A7-Foil only exposed the Ti foil plates on the face of the sample, leaving undamaged C12A7:e^- in the sample interior. In this sample, the high electrical conductivity (higher than C12A7-C and C12A7-TiB_2) must be attributed to high electron mobility through C12A7:e^-. As will be discussed in CH. 5, the electron density of C12A7-Foil is found to be on the order of 1E21/cm^3, or near theoretical maximum. The electron mobility in C12A7-Foil may also be higher than that of the composite samples due to C12A7:e^- grain growth during sintering.[19] Although grain size was not measured in this work, it is reasonable to hypothesize that the average C12A7:e^- grain size is larger in C12A7-Foil compared to the composite samples due to the absence of grain boundary pinning by secondary phases.[45]

Despite that the conductive reinforcing phase is less than 30 vol%, C12A7-C and C12A7-TiB_2 yet exhibit appreciable conductivities. Previous studies showed that in a non-ideal system, segregation of the insulative and conductive phases leads to a reduction of the threshold vol% as phase connectivity occurs at a higher possibility if the conductive phases are locally clustered.[46,47] Segregation of the conductive reinforcing phases was observed in the cross-section microstructure of the composites, as shown in Figure 3.1. An additional explanation for the reduction in apparent threshold vol% for the CB and TiB_2 composites may lie in the different particle sizes of the insulative and conductive phases. As the particle size ratio of insulator to conductor increases, the threshold vol% decreases, as the smaller conductive particles will fill the interstices between the larger insulative particles and form a phase-segregated system. The CB and TiB_2 powders used in

this study were both micron-sized, however the preformed C12A7 essentially sinters during heat treatment and must be subsequently ground in a mortar and pestle, which results in a particle size that is an order of magnitude larger than the reinforcing particles. Porosity also affects the conductivity of a composite as pores are essentially an insulative phase. However, the pore effect is negligible in this study because of the high densities of the composites.

3.3 Phases and Microstructure

XRD patterns of the as-sintered samples are shown in Figure 3.3. C12A7-P, C12A7-C, and C12A7-Foil exhibit virtually identical XRD patterns, with all the peaks corresponding to C12A7 or C12A7:e^- phase. It is worth noting that there is no difference between the XRD peaks for the insulative C12A7 phase and those for the C12A7:e^- electride phase. No decomposition of C12A7 occurred in C12A7-P, C12A7-C, or C12A7-Foil, as no other calcium aluminate phases are observed in the XRD patterns. However, C3A and CA are found in C12A7-Ti and C12A7-TiB_2, respectively. In addition, Ti_2Al and TiC are observed in C12A7-Ti. The formation of these other calcium aluminate phases is to be discussed in the next section when EDS results are present.

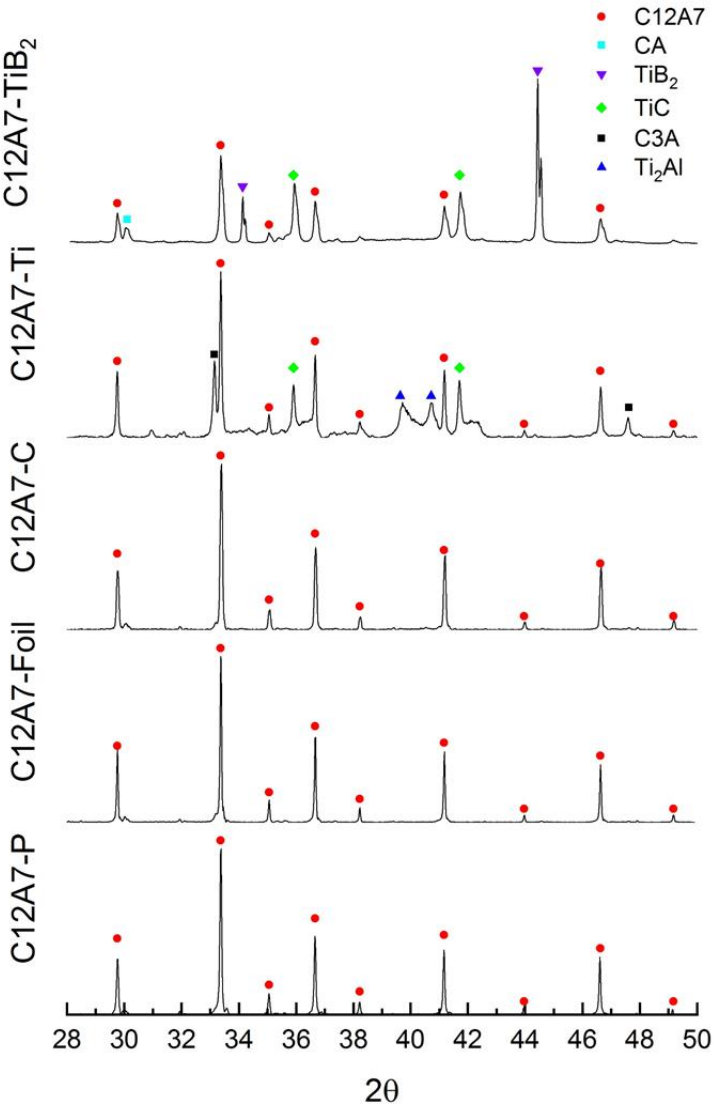

Figure 3.3: XRD patterns of sample surfaces

Representative microstructures of the as-sintered samples are shown in Figure 3.4. The pore size is on the order of several microns in C12A7-P and C12A7-Foil. Cracks and large pores are observed in C12A7-Ti, although the relative density is 99%. These cracks and pores were formed due to the pull-out of the reaction layers at the C12A7-Ti interface during sample preparation processes (mechanical grinding and polishing), as the fracture surfaces of C12A7-Ti

(Fig. 3.5d) show flush interfaces. It is worth noting that the insulative C12A7 phase (Fig. 3.4a C12A7-P) and the C12A7:e^- electride phase (Fig. 3.4b C12A7-Foil) did not show any visible difference in SEM. No conductive coating was required for imaging C12A7-P in SEM.

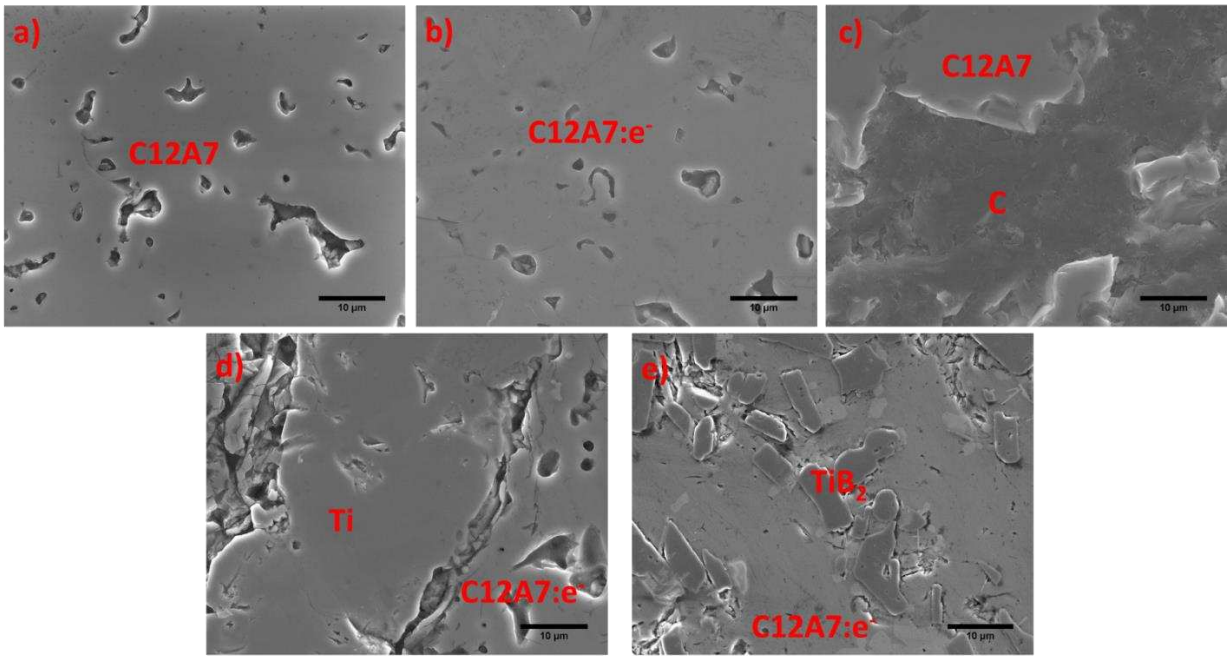

Figure 3.4: SEM images of sample cross-sections: a) C12A7-P b) C12A7-Foil c) C12A7-C d) C12A7-Ti e) C12A7-TiB_2

Figure 3.5 displays the fracture surface of each sample. The C12A7 phase and the C12A7:e^- electride phase look identical in all the samples except those in C12A7-Ti, in which a non-conductive phase is present at the C12A7:e^--Ti interface. There is a white, spiderweb-like pattern across the C12A7:e^- fracture surface at the interface (Fig. 3.6) in sample C12A7-Ti. The fracture surfaces observed in the other four samples are consistent with what were reported in literature.[34]

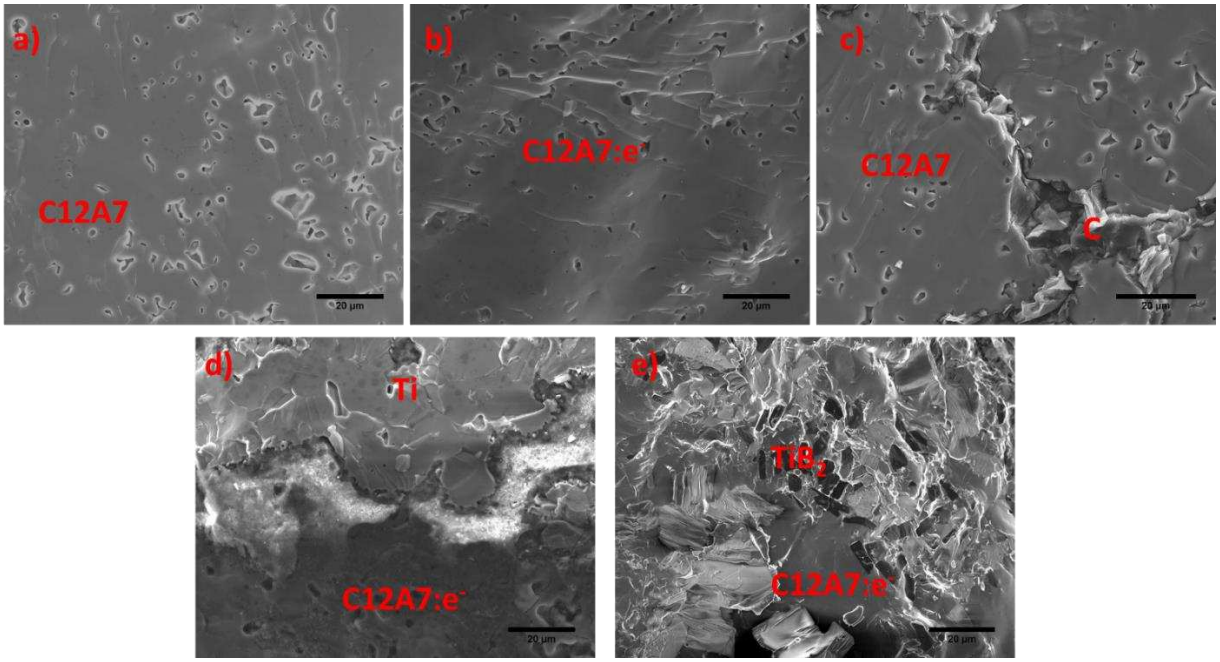

Figure 3.5: SEM images of sample fracture surfaces: a) C12A7-P b) C12A7-Foil c) C12A7-C d) C12A7-Ti e) C12A7-TiB_2

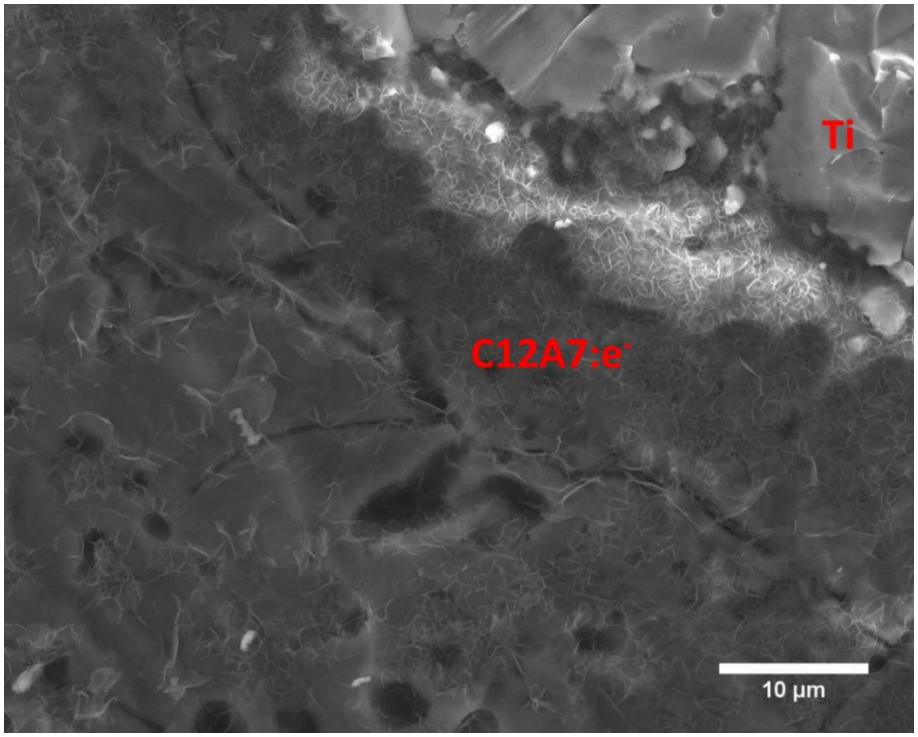

Figure 3.6: Fracture surface of C12A7:e^- in C12A7-Ti displaying web-like pattern

To investigate the non-conductive (white) phases at the C12A7-Ti interface, EDS line scanning was performed across the C12A7:e^--C and C12A7:e^--Ti interfaces, the results of which are shown in Figure 3.7 and Figure 3.8, respectively. In C12A7:e^--C, little diffusion of any C12A7 constituents into the carbon region was observed. There is also some diffusion of carbon into the C12A7:e^- region. In contrast, Al is leached from the C12A7:e^- region and diffuses to the Ti region with a diffusion path of several microns. No appreciable quantities of O are detected in the Ti region, suggesting the formation of pure intermetallic Ti_2Al.[48]

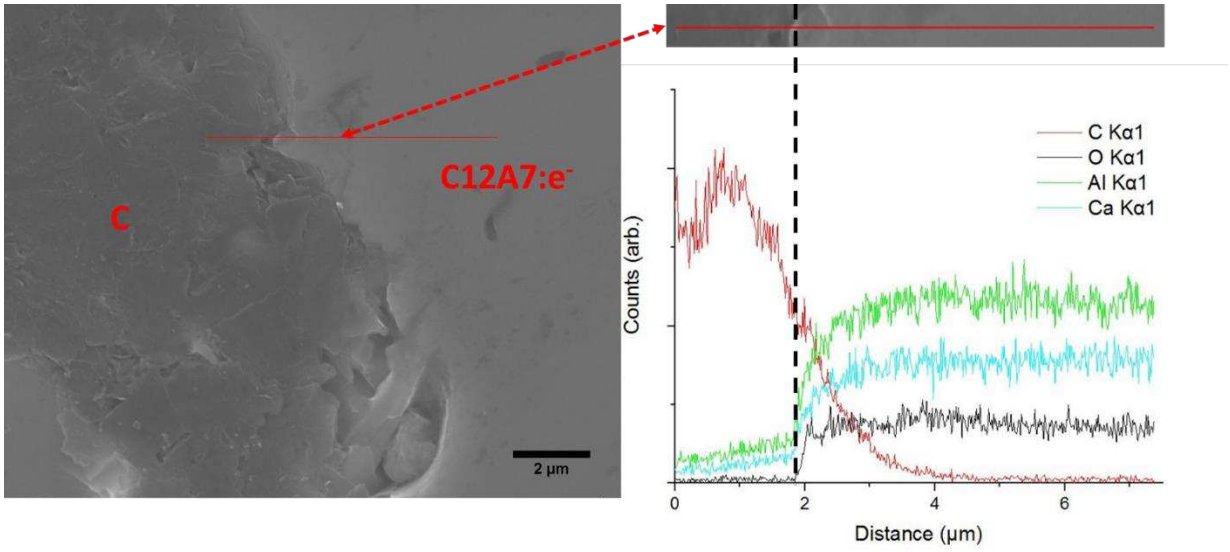

Figure 3.7: Line scan across C12A7:e^--C interface showing C diffusion into C12A7:e^-

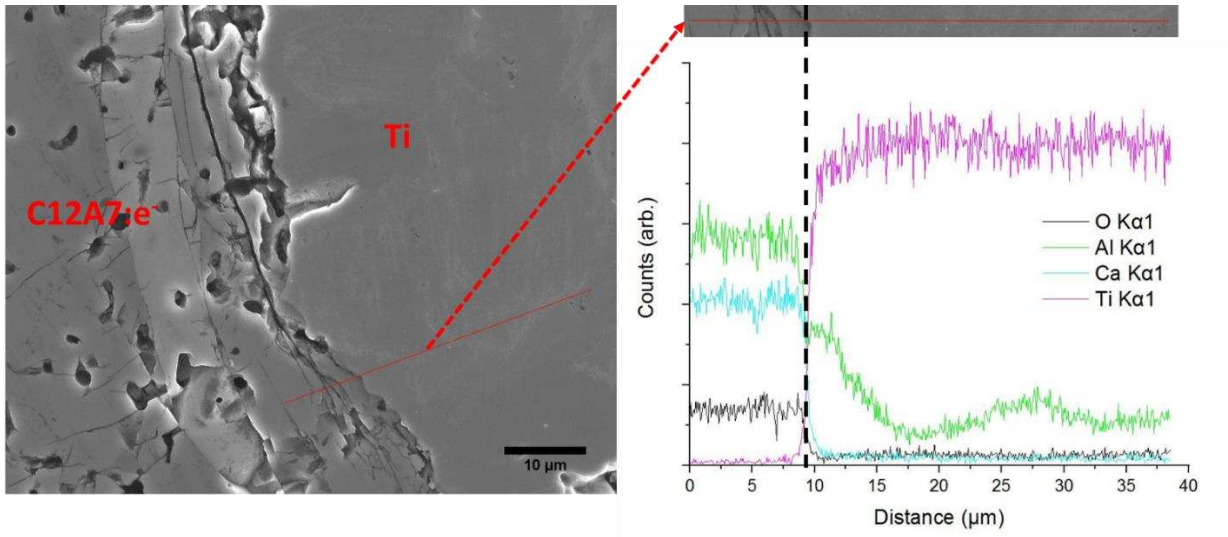

Figure 3.8: Line scan across C12A7:e$^-$- Ti interface showing Al diffusion into Ti

3.4 Discussion

As the oxy-mayenite (insulative) and the C12A7:e$^-$ electride phase do not exhibit noticeable differences in either XRD or SEM, the color of the samples is typically used to preliminarily study the effectiveness of reducing C12A7 to C12A7:e$^-$. Insulative C12A7 is white, as was observed in C12A7-P. As C12A7 converts to C12A7:e$^-$, the color changes from white to green to black, as was observed in C12A7-Foil. In C12A7-C, C12A7-Ti, and C12A7-TiB_2, large particles of C12A7 and C12A7:e$^-$ are surrounded by networks of the corresponding reinforcing phases. The comparison of the cross-section microstructures of C12A7-C, C12A7-Ti, C12A7-TIB_2, and C12A7-Foil suggests that Ti is a more effective reducing agent as a higher amount of C12A7 is converted to C12A7:e$^-$. From the color change in sample C12A7-C, some regions have only undergone partial reduction and primary regions consist of C12A7 phase. Formation of C12A7:e$^-$ in C12A7-TiB_2 is retarded by the formation of a protective oxide layer on the surface of the TiB_2 particles.[42]

The different behavior in electride formation in the various samples is attributed to the nature of each reduction reaction involved. In C12A7-Ti, Ti has a strong oxygen affinity at high

temperatures as shown in an Ellingham diagram (to be discussed in more detail in CH. 4).[49] Thereby the clathrated O^{2-} anions are prone to be extracted from the cage structure in C12A7 and electrons from the Ti or from the SPS process are able to rapidly replace the extra-framework O^{2-} anions to form C12A7:e-. In C12A7-C, C must first diffuse into C12A7 in order to bond with the O^{2-} anions and form CO or CO_2. In the case where preformed C12A7 powder has a large particle size, a substantial amount of time is required to enable complete diffusion of C through the particles. Further size reduction of the preformed C12A7 particles combined with more intimate blending with carbon black particles may improve the formation of C12A7:e^- in C12A7-C .

Several secondary phases are observed in C12A7-Ti. The formation of these phases resulted from two separate processes during SPS. The first process is the carbothermal reduction of TiO_x that lead to the formation of the TiC. The second process is the leaching of Al by Ti during SPS. As discussed earlier, the reduction of C12A7 by a metal leads to the formation of a metal oxide layer on the surface of C12A7. In the case of Ti, this can lead to the formation of a wide range of oxides, including TiO_2, Ti_3O, and Ti_2O_5.[38,50] As TiO_x particles are heated above 1087°C in close contact with C, the oxides will be reduced following a series of reactions and finally lead to:

$$TiO_2(s) + 3C(s) \rightarrow TiC(s) + 2CO(g) \qquad \text{Equation 3.1}$$

In C12A7-Ti, increased outgassing is observed above 1100°C, as shown in Figure 3.9.[51]

The formation of C3A and Ti_2Al are both tied to the same process. It has been shown elsewhere that consolidating Al_2O_3-Ti composites via SPS leads to the formation of intermetallic $Ti_3Al[O]$.[52] The growth of TiAl intermetallic phases was accelerated in the presence of an applied electric field.[53] These findings, coupled with the XRD and EDS data presented here, support the conclusion that Ti is leaching Al from C12A7 to form intermetallic layers in the composite. As Al

is leached from C12A7, the calcium-rich phase C3A is formed.[40] It is worth noting that this decomposition reaction is not observed in C12A7-Foil.

The secondary phases observed in C12A7-TiB_2 resulted from the oxidation of TiB_2, which lead to the formation of both TiO_x and B_2O_3.[42] B_2O_3 melts at 450°C, and volatizes around 1000°C.[54,55] CaO forms a liquid phase with B_2O_3 below 1000°C,[56] while Al_2O_3 does not interact with B_2O_3 readily.[57] As a consequence, C12A7 is readily decomposed to a Al_2O_3-rich CA phase as the CaO is leached out and reacts with B_2O_3 to form a melt that subsequently volatize at a temperature ~1000°C, when TiB_2 is used to reduce C12A7 during SPS. The formation of TiC in C12A7-TiB_2 is attributed to the reaction described in Eqn. 3.1, above.

The outgassing phenomenon was investigated by monitoring the SPS chamber pressure (Fig. 3.9), which provides qualitative information to support the reduction reactions discussed previously. The reduction of C12A7 by C is proposed[37] as:

$$C_2^{2-}(\text{cage}) + 2O_2^{2-}(\text{cage}) \rightarrow 2CO(\text{atmosphere}) + 6e^-(\text{cage}) \qquad \text{Equation 3.2}$$

Sintering of C12A7-C involves the largest amount of gas at high temperature, as the reduction reaction by carbon is accompanied by outgassing as shown in Eqn. 3.2. Also, the diffusion of C into C12A7 is dependent on the contact-area. In contrast, most of the reduction is completed by the formation of a TiO_x layer during the sintering of C12A7-Ti. Therefore, a low amount of gas is involved while sintering this sample, and what little is generated above 1100°C may be attributed to the formation of TiC, as discussed above.

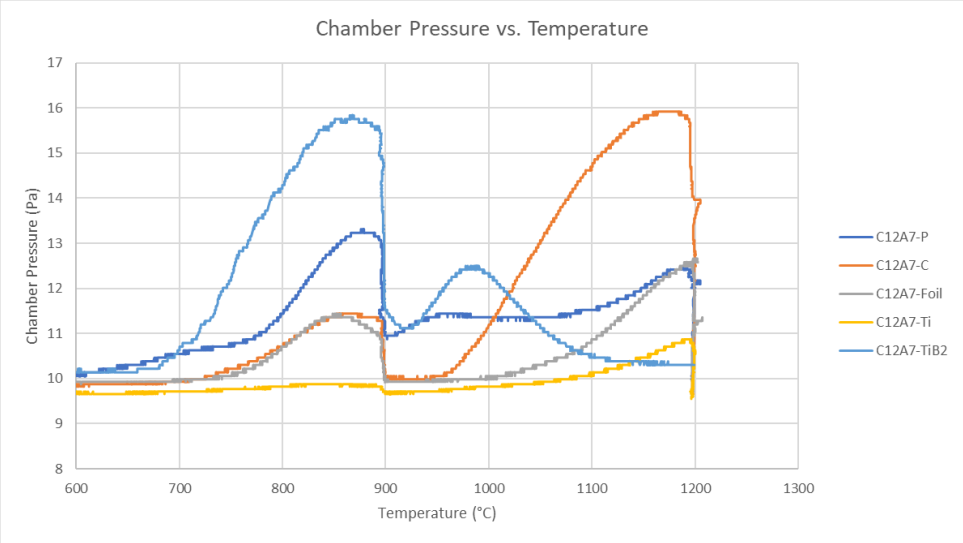

Figure 3.9: SPS chamber pressures vs. temperature

Chapter 4 Fabrication of Mayenite and Mayenite Electride via *In-Situ* Reaction Sintering

Most studies on the fabrication of bulk mayenite (C12A7) used preformed C12A7 powder as the starting materials. In CH. 3, we addressed the effect of adding reinforcing phase to the preformed C12A7 powder on the phase formation and microstructure in the bulk samples. One of the objectives to investigate SPS for C12A7 or mayenite electride (C12A7:e^-) fabrication is the fast sintering rate, i.e., time saving. Although the preformed C12A7 powder approach is effective to form bulk C12A7, the process to prepare C12A7 powder is very time consuming (on the order of 24 to 36 hours).[58] Therefore, this chapter focuses on an alternative processing route that uses *in-situ* reaction in SPS, which has not been attempted/published. The effect of precursor powder, heating rates and addition of conductive particles to precursor powder on the phase formation are to be discussed in this chapter.

4.1 Precursor Powder for *In-Situ* Reaction Sintering

To investigate the viability of *in-situ* reaction sintering of bulk C12A7 and C12A7:e^-, the ball milled (ten-minute milling time) precursor powders used to generate the preformed C12A7 powder in CH. 3 were directly used as feedstock in SPS. Sintering parameters identical to those used in the study of preformed C12A7 were applied as the starting point for comparison purposes. Unfortunately, this initial attempt was aborted as the feedstock material was ejected out of the die and into the SPS machine when the temperature was raised above 1000°C. This suggested that the one-minute outgassing period at 900°C did not provide enough heat to the powder compact to allow for complete decomposition of $CaCO_3$. As a result, the force of outgassing at higher

temperatures pushed the material out of the graphite die. To account for this, the outgassing hold was modified from one minute at 900°C to six minutes at 1000°C.

This modification of the outgassing period was successful in terms of eliminating the ejection issue. However, the sample fractured when it was removed from the die, indicating that different SPS parameters needed to be explored for *in-situ* reaction sintering. Figure 4.1a shows the geometry of the largest contiguous piece of the fractured sample. Figure 4.1b shows the XRD pattern of the sample interior, which primarily consists of C12A7 phase. The dark green color of the sample suggested that some C12A7:e^- had formed. This sample is referred to C12A7-R1 hereafter.

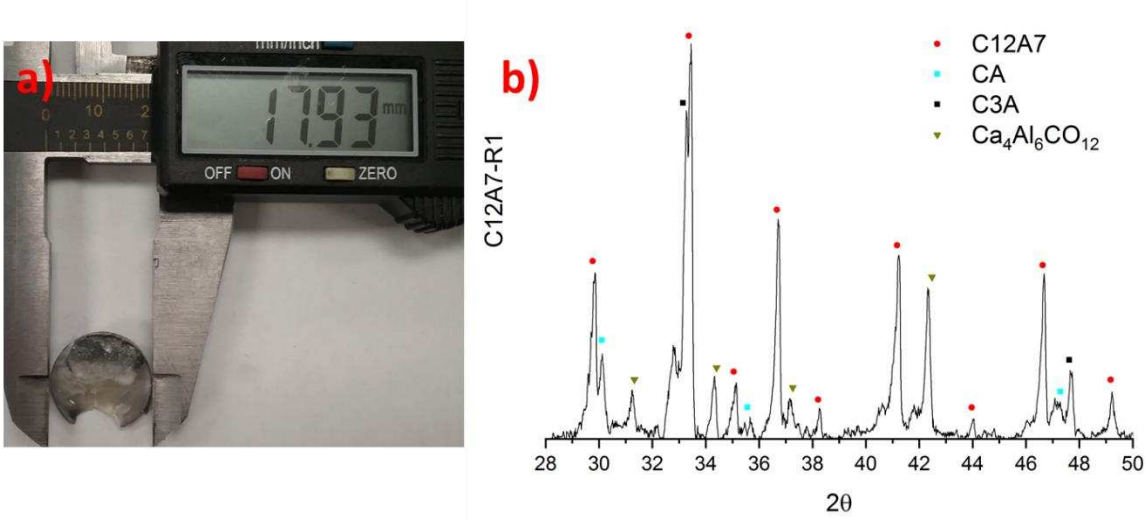

Figure 4.1: C12A7-R1 a) optical image of largest contiguous piece b) XRD pattern

While this first attempt of *in-situ* reaction sintering was promising, the XRD pattern shows that large quantities of secondary calcium aluminate phases are present in the sample. In addition, a sodalite-based structure that is tentatively labelled as $Ca_4Al_6CO_{12}$ (soda-aluminate) was identified, which will be discussed in detail in Section 4.2.[59] The formation of the undesired phases may result from insufficient mixing of the precursor powders to form C12A7 in such a short sintering time (ten minutes).

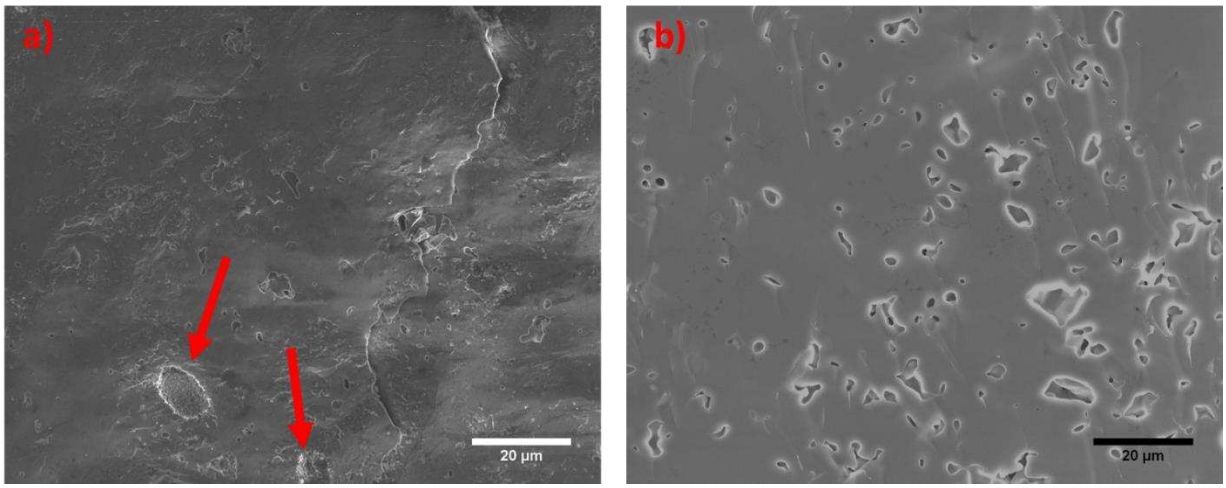

Figure 4.2: SEM images of fracture surface of a) C12A7-R1 b) C12A7-P

The interior fracture surface was examined in SEM to characterize the microstructure and to identify origin of fracture (Fig. 4.2). Though the origin of the fracture was not clearly shown, the uniform pore structure in the preformed C12A7 sample (C12A7-P) was not observed in C12A7-R1; This first sample produced by *in-situ* reaction sintering was fully dense except for a small number of large pores containing unreacted particles, as highlighted by the arrows in Figure 4.2a. This observation led to the hypothesis that the chemical composition gradient between the CaO and Al_2O_3 particles provide a much stronger diving force for mass transport compared to the reduction of interfacial area, which is the force responsible for densification while sintering chemically homogeneous powder compacts.[33]

As it was hypothesized that the chemical composition gradients in the $CaCO_3$-Al_2O_3 system would drive densification, the applied pressure was reduced from 30 MPa to 10 MPa (minimal contact pressure) for the 2nd attempt of *in-situ* reaction sintering, the sample of which is referred to as C12A7-R2 hereafter. Sample C12A7-R2 was successfully removed from the die without fracturing into multiple pieces. Figure 4.3 shows the dimensions and color of the sample

C12A7-R2 and an optical image of the top surface. Refer to Figure 4.3d for clarification as to what is meant by top and bottom surface.

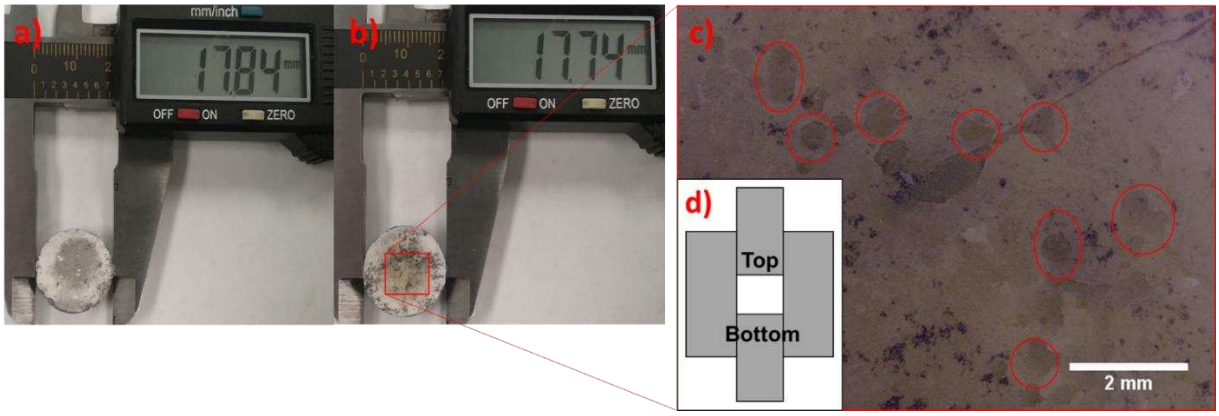

Figure 4.3: Pictures of sample C12A7-R2 a) bottom surface, b)top surface, and c) optical image of top face showing surface porosity d) inset, schematic distinguishing top and bottom of SPS configuration

There are several millimeter-sized pores on the top surface of the sample while the bottom surface was dense. The large pores present in the sample surface resulted from the trapped gas bubbles that were not pressed out of the sample during sintering. XRD of both surfaces (Fig 4.4) revealed that the top porous surface contained primarily C12A7, while the bottom dense surface contained primarily secondary calcium aluminate phases.

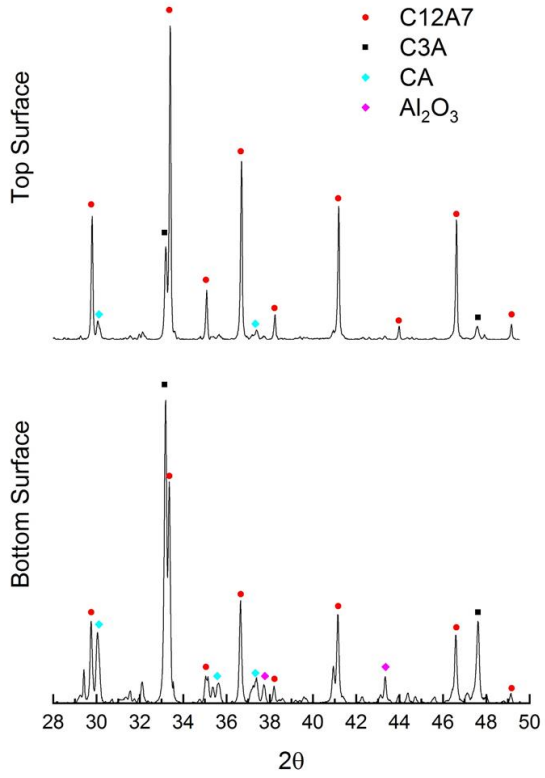

Figure 4.4: XRD of top and bottom surface of C12A7-R2 showing inhomogeneous calcium aluminate formation

Based on the results of these two initial attempts, it was necessary to improve the mixing of the precursor powders to efficiently form C12A7 or C12A7:e^- via *in-situ* reaction SPS. Therefore, stoichiometric precursor powders were ball milled for extended time length: two and ten hours. Powders ball milled for different times will be denoted as 10Min. BM, 2Hr. BM, and 10Hr. BM. It is worth noting that non-negligible amounts of Al_2O_3 are abraded away from the milling jars and balls into the precursor powders during extended milling times. Thus, the initial 12:7 stoichiometric mass ratio of CaO:Al_2O_3 decreases as ball milling time increases. To study the amount of Al_2O_3 added to the powders, XRD was performed on the precursor powders to track the relative intensities of the Al_2O_3 and $CaCO_3$ peaks (Fig. 4.5). As expected, the intensities of the Al_2O_3 peaks increased as milling time was extended. Significant broadening of the $CaCO_3$ peaks

was also observed as the milling time was extended, indicating that the $CaCO_3$ powders had been reduced to nanometric sizes.[60]

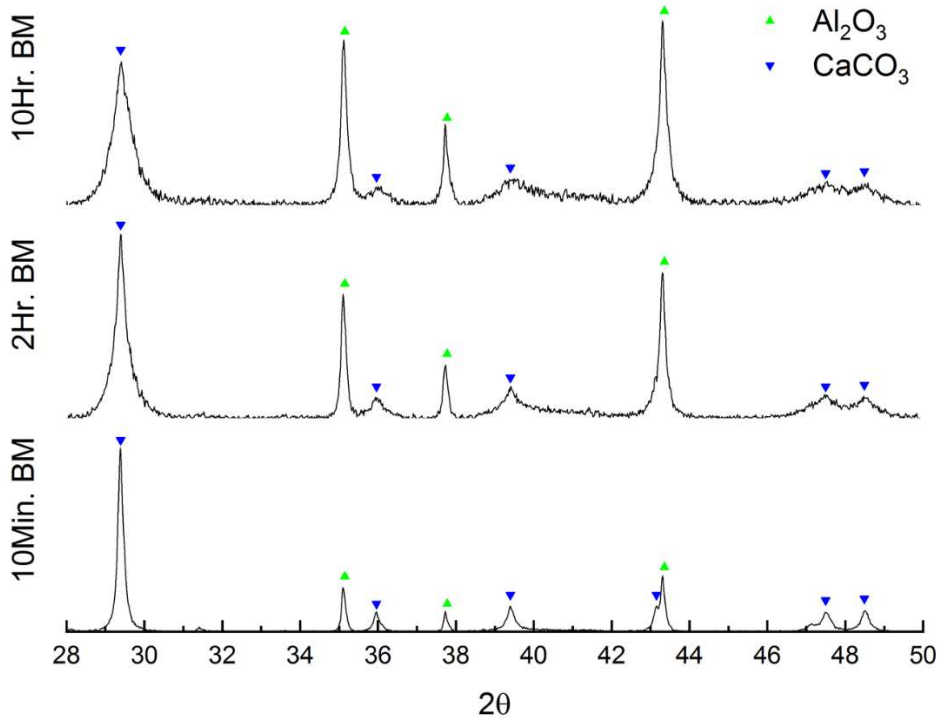

Figure 4.5: XRD patterns of precursor powders ball milled for various times

Thermogravimetric/differential thermal analysis (TG/DTA) is performed on the precursor powders to investigate if the ball milling time length has any effect on the formation of calcium aluminate phases. As shown in Figure 4.6, two reactions occurred during heating. The endothermic peak at 750°C corresponds to the decomposition of $CaCO_3$. This reaction is easily identified by the accompanying mass loss.[61] In addition, an exothermic peak is observed at approximately 930°C. While no specific reference to this exothermic peak has been found in literature, it is known that the enthalpies of formation of all calcium aluminate phases are negative, meaning that any formation reaction would be exothermic.[23] From this set of experiments, it was determined that calcium aluminate phase formation initiates above 930°C. The intensity of the exothermic peak,

i.e., the heat generated by this reaction, is far greater for 2Hr. BM and 10Hr. BM than for 10Min. BM.

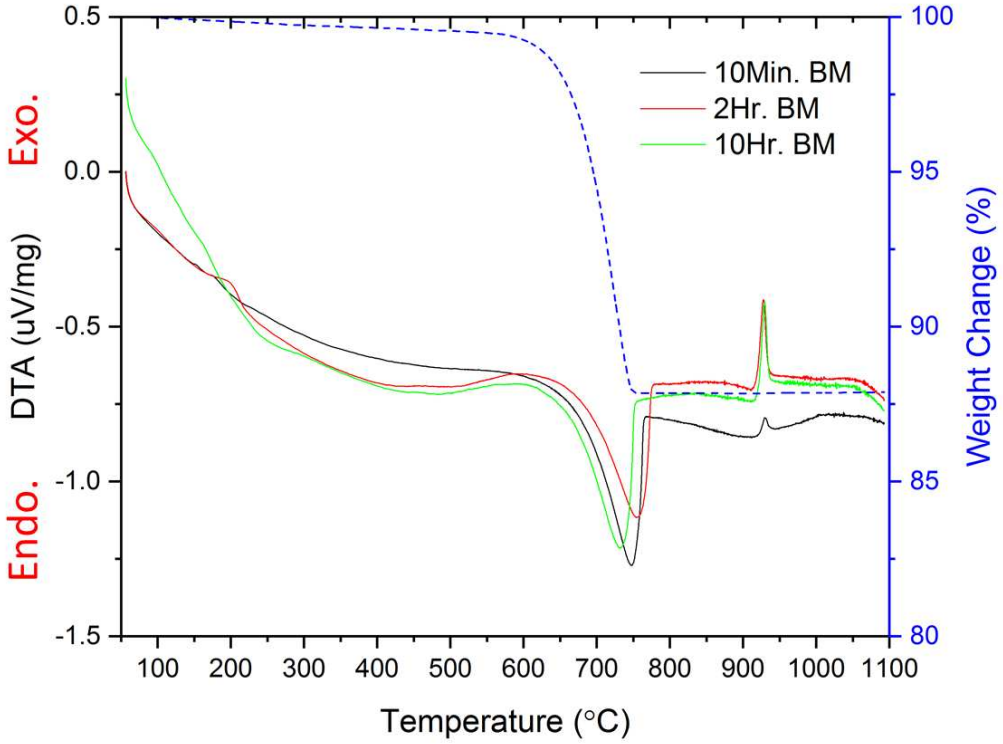

Figure 4.6: TG/DTA plots of the different precursor powders that were ball milled for ten minutes, two hours, and ten hours

XRD characterization (Fig. 4.7) of the post-thermal-analysis powders suggest that the higher intensity of the exothermic peaks for 2Hr. BM and 10Hr. BM are attributed to the formation of higher amounts of calcium aluminate phases (CA, C3A and C5A3).

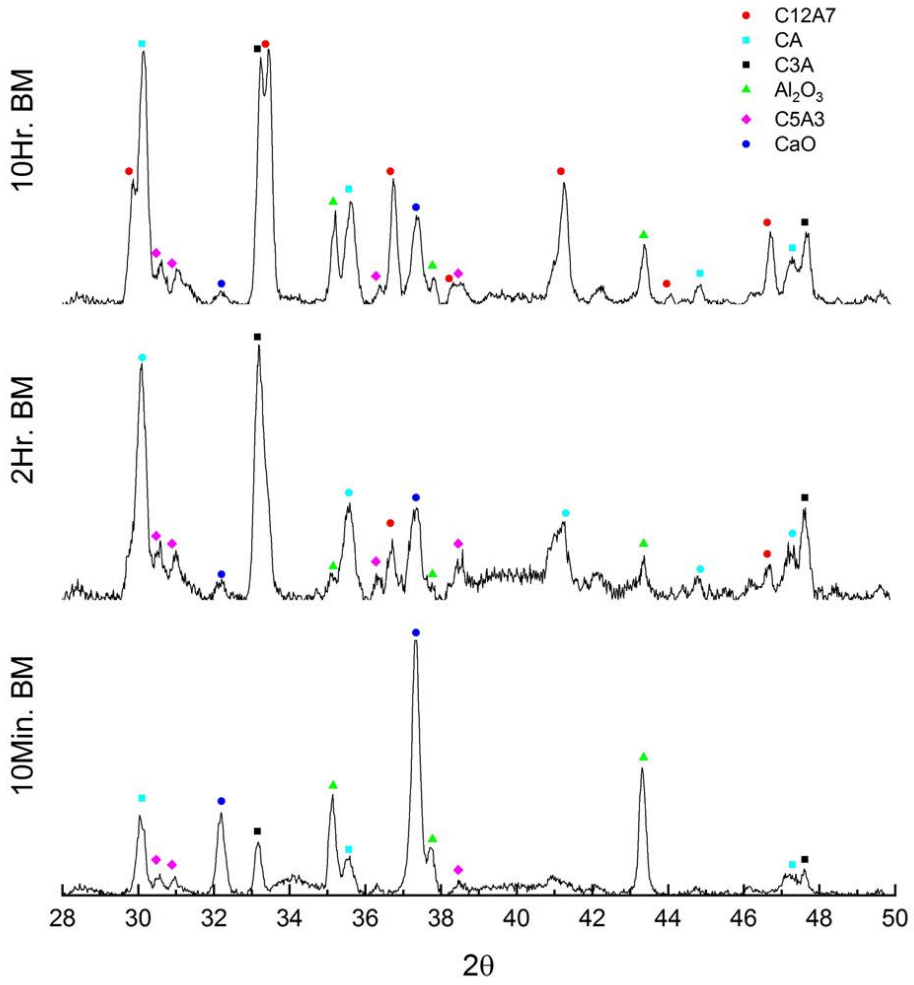

Figure 4.7: XRD patterns of precursor powders post TG/DTA

An in-depth review on the effect of precursor chemical homogeneity on the rate of calcium aluminate formation has been performed by Salasin and Rawn.[24] The formation of calcium aluminates is mediated by the diffusion of Ca into Al_2O_3. Therefore, when the precursor powders are highly chemically heterogeneous, such as 10Min. BM, the formation of calcium aluminates is initially rapid but subsequently stunted due to the long diffusional distances that Ca must travel as the reaction proceeds. Longer ball milling time improves the chemical homogeneity in the

precursor powders. Therefore, the calcium aluminate formation reactions can proceed in a shorter time frame in 2Hr. BM and 10Hr. BM.

It has now been demonstrated that there is merit to using extended ball milling times, as it accelerates the rate of calcium aluminate formation. However, while extended milling times increase the rate of calcium aluminate formation, the addition of excess Al_2O_3 from the jars and media leads to the formation of a substantial amount of CA, in addition to C12A7. To maximize C12A7 formation, the excess Al_2O_3 must be accounted for. To try to quantify the amount of excess Al_2O_3 added to the precursor powders, the ball milled powders were all subjected to the same heat treatment used to form C12A7. XRD of the powders after heat treatment confirmed that a non-negligible quantity of CA formed. An elementary approach was used to identify the amount of excess $CaCO_3$ required to suppress CA formation in powders that were ball milled for two and ten hours. The precursor powders were weighed before and after heat treatment. Presumably all mass loss is attributed to the release of CO_2 gas from the decomposition of $CaCO_3$. As the molar ratio between CO_2 and $CaCO_3$ is 1:1 in the decomposition reaction, the initial masses of $CaCO_3$ and Al_2O_3 in each powder mixture can be calculated. Subsequently, the amount of excess Al_2O_3 present in the powder mixture is determined and the mass of $CaCO_3$ powder needed to maintain the 12:7 molar ratio between CaO and Al_2O_3 can be calculated. Using the mass measurements from the initial 2Hr. BM and 10 Hr. BM powders, the mass of the $CaCO_3$ powder in the feedstock for ball milling is adjusted to account for the unintentional addition of Al_2O_3 from the milling media to maintain the 12:7 molar ratio of CaO:Al2O3. $CaCO_3$-adjusted powders will be denoted as 2Hr. BM-A and 10Hr. BM-A. Heat treatment was conducted on the adjusted powder after ball milling. XRD patterns of the adjusted preformed C12A7 powders confirmed that CA formation was suppressed in both 2Hr. BM-A and 10Hr. BM-A, as shown in Figure 4.8. 10Min. BM powder was

non adjusted as CA was not observed after heat-treatment. Adjustment was only required for the powders that were ball milled for extended times, such that the 12:7 stoichiometry was changed by the addition of Al_2O_3.

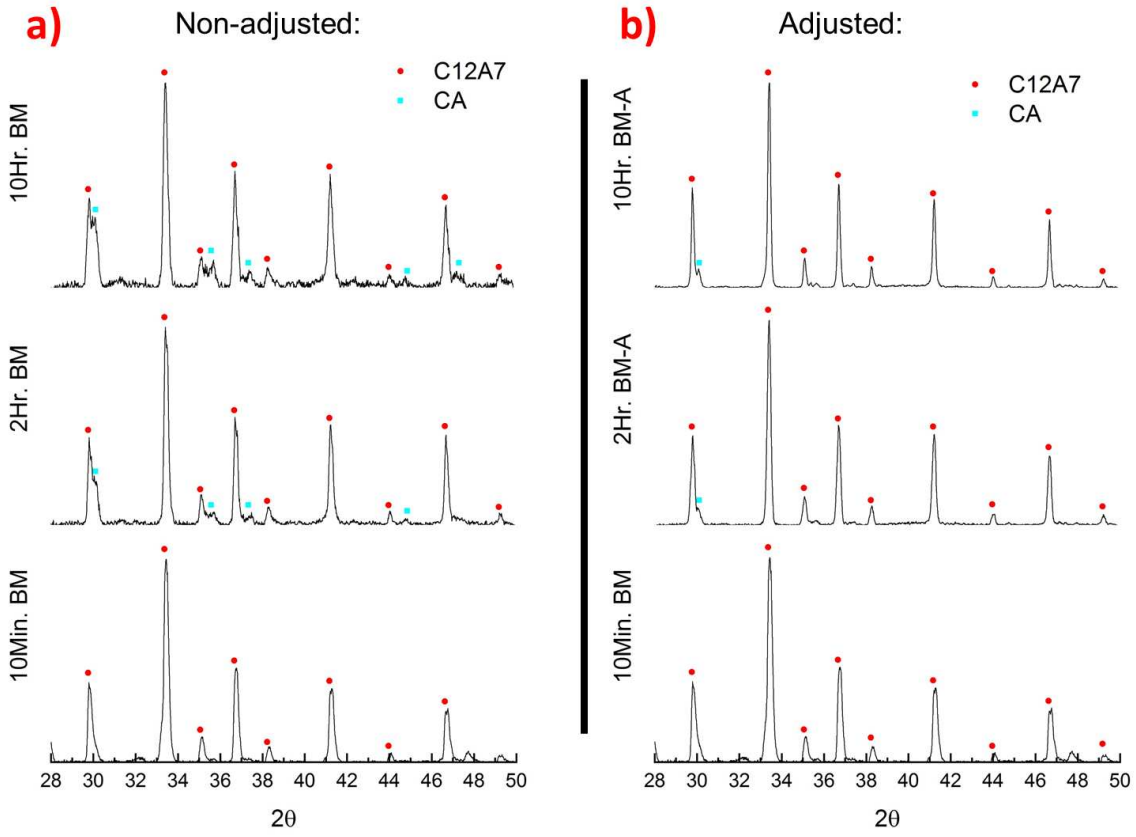

Figure 4.8: XRD patterns of heat-treated powders a) non-adjusted b) adjusted powders

Non-adjusted ten-hour ball milled powder was used to sinter sample C12A7-R3 as a baseline to compare to the samples made from the adjusted ball milled powders. The hypothesis was that the samples made from adjusted ball milled powders would contain C12A7 and CA in quantities similar to those observed in the non-adjusted heat-treated powders, if the precursor homogeneity was increased. The sample (C12A7-R3) was extracted from the SPS without fracture and did not exhibit any macroscopic porosity (Fig. 4.9a). XRD showed that sample C12A7-R3 consists of C3A and a soda-aluminate phase $Ca_4Al_6SO_{12}$ (Fig. 4.9b). Research into the structure of

this compound was performed by Brenchley and Weller, who formed the compound of interest via the reaction:

$$Ca_{64}[Al_{96}O_{192}](SO_4)_{16} \rightarrow 8Ca_8[Al_{12}O_{24}]\bullet S_2 + H_2O \qquad \text{Equation 4.1}$$

whereby the sulfate is reduced by H_2 at 900°C.[59] While this group particularly focused on sulfate-based sodalites, they acknowledged that carbonate-based structures constructed around C^{2-} anions had also been produced. Considering this acknowledgement, and the absence of S in this study, it is proposed that the phase formed in C12A7-R3 is $Ca_4Al_6CO_{12}$. An analysis of the stoichiometry of C12A7 and its precursors shows that the occurrence of the soda-aluminate phase with C3A may be expected.

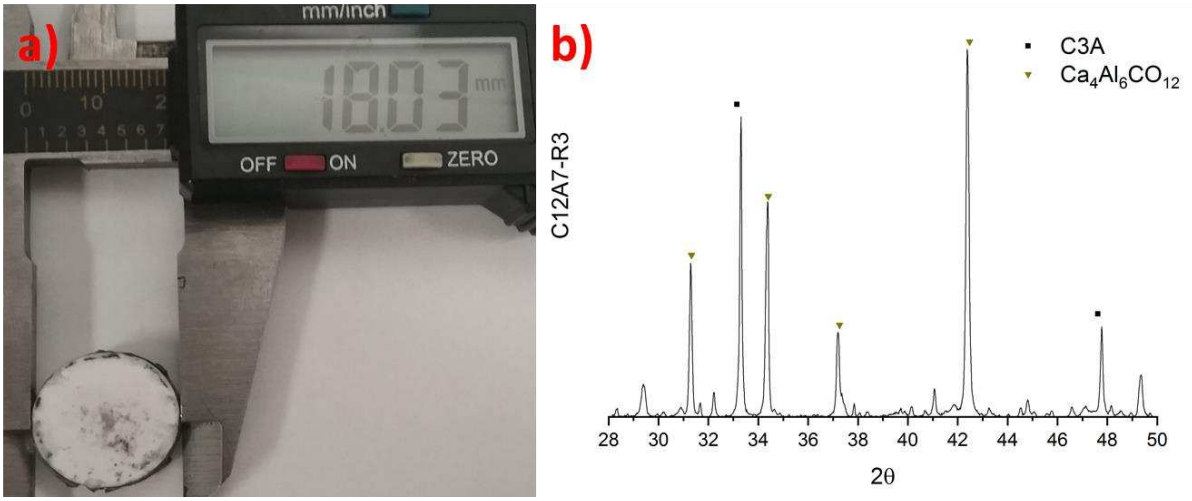

Figure 4.9: C12A7-R3 a) optical image b) XRD pattern

The precursor powders are mixed such that after the decomposition of $CaCO_3$ to CaO, the resultant stoichiometry equals $Ca_{12}Al_{14}O_{33}$ (C12A7). To satisfy this, the precursor powders must have the stoichiometry $Ca_{12}C_{12}Al_{14}O_{57}(12CaCO_3\bullet 7Al_2O_3)$. The formation of one mole of soda-aluminate from the precursor powders yields:

$$Ca_{12}C_{12}Al_{14}O_{57} - Ca_8C_2Al_{12}O_{24}(\text{soda-aluminate}) = Ca_4C_{10}Al_2O_{33} \qquad \text{Equation 4.2}$$

The right-hand side of Eqn. 4.2 then forms one mole of C3A (Eqn. 4.3), which leaves behind CaO and gaseous products (Eqn. 4.4).

$$Ca_4C_{10}Al_2O_{33} - Ca_3Al_2O_6(C3A) = CaC_{10}O_{27} \quad \text{Equation 4.3}$$

$$CaC_{10}O_{27} \rightarrow CaO + 10CO_2 + 3O_2 \quad \text{Equation 4.4}$$

While this analysis assumes perfect stoichiometry of the precursor powders, this sample was sintered using the CaO-deficient powders, which may explain why the remaining CaO in Eqn. 4.4 is not observed in XRD. Both the analysis above and the experimental results implied that calcium aluminate formation occurred prior to the completion of $CaCO_3$ decomposition in SPS. This implication will provide the basis for experimentation performed in Sections 4.2 and 4.3.

Two samples were sintered via *in-situ* reaction using the adjusted powder: C12A7-R4-2Hr, and C12A7-R4-10Hr, corresponding to 2Hr. BM-A and 10Hr. BM-A, respectively. These samples were compared to C12A7-R2, as it was sintered using 10Min. BM powder and otherwise identical conditions. While the bottom surfaces of these three samples were virtually identical, porosity on the top surface was remarkably reduced in sample C12A7-R4-2Hr and practically eliminated in sample C12A7-R4-10Hr, as shown in Figure 4.10. The reduction in porosity is attributed to more efficient powder packing in the powders ball milled for longer times. XRD patterns revealed that the top surface of each sample exhibited dominant C12A7 phase and minor CA phase, while the bottom surface of each sample contained relatively higher amounts of CA, C3A, and Al_2O_3 (Fig. 4.11).

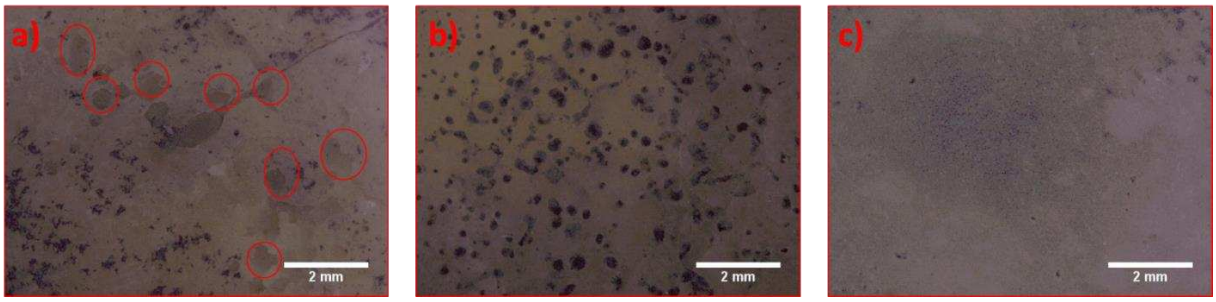

Figure 4.10: Optical images of the surface of the samples sintered via *in-situ* reaction a) C12A7-R2 b) C12A7-R4-2Hr c) C12A7-R4-10Hr

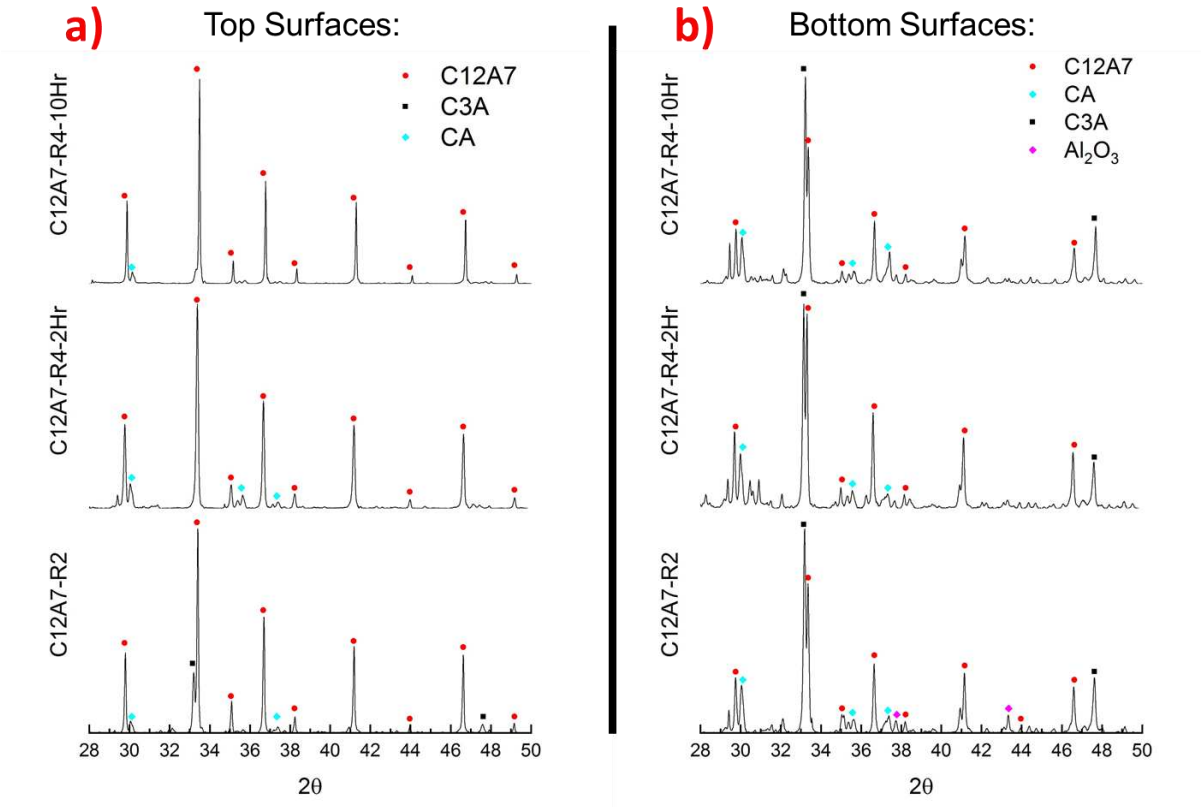

Figure 4.11: XRD patterns of a) top and b) bottom surfaces of *in-situ* samples sintered under identical conditions

4.2 Effect of Heating Rate in SPS

To understand the mechanism of the formation of the secondary calcium aluminate phases, it is important to investigate the heat transfer during the sintering and the actual temperature distribution in the sample. In section 4.1, it was found that the formation of calcium aluminates, which initiated at approximately 930°C, occurred concomitantly with the decomposition of $CaCO_3$. When $CaCO_3$ decomposition occurs concurrently or later than the formation of calcium aluminates there are two possible outcomes. In the case where powders are packed efficiently (C12A7-R3), a soda-aluminate phase is formed. In the case where powders are packed inefficiently (C12A7-R2), the entrapment of gas may lead to the formation of large pores and subsequent fracture of the sample. In either case, the presence of CO_2 during calcium aluminate formation is detrimental to C12A7 formation. From literature, the decomposition of $CaCO_3$ to CaO and CO_2 occurs at a maximum rate at 800°C.[61] When the sintering temperature is set above 1000°C, it is anticipated that the *in-situ* reaction of CaO and Al_2O_3 to form calcium aluminates should occur after the decomposition of $CaCO_3$. However, as there appeared to be an incongruency between these reactions in SPS, a more thorough investigation of heating effects in SPS seemed appropriate.

The true temperature distribution in the samples deviates from the temperature measured/recorded by a pyrometer during SPS, which is targeted at a blind hole in the graphite die and measures the temperature at that point. Generally, it is assumed that the temperature measured by the pyrometer is equal to the sample temperature in SPS experiments, but in reality, this is not the case. As discussed in CH. 1, heat is generated in SPS via Joule heating, which occurs when current passes through an object. Graphite is conductive while C12A7 and its precursors are insulative. Therefore, the electric current travels through the graphite die rather than the C12A7

precursor. When there is no current passing though the powder compact, it gains heat through thermal conduction from the surrounding graphite tooling. Thus, the powder compact does not experience the same rapid heating as the graphite die. As a result, large temperature gradients are present between the sample and the graphite die, which potentially lead to the incomplete decomposition of $CaCO_3$ when the reaction of CaO and Al_2O_3 occurs. In addition, high heating rates, such as those typically used in SPS (~ 100°C/min or above), may increase the onset temperature of a chemical reaction, known as the Kissinger effect. Kissinger et al. found that the onset temperature of $CaCO_3$ decomposition increased from 871°C to 927°C when the heating rate was increased from 3°C/min to 12.5°C/min.[62]

To investigate the effect of fast heating rates in SPS on the reactions of $CaCO_3$ decomposition and calcium aluminate formation, TG/DTA was performed on 10Hr. BM powder with different heating rates: 5°C/min, 10°C/min, 20°C/min and 50°C/min. Higher heating rates were not studied due to the limitation of the TG/DTA equipment; 50°C/min is the maximum heating rate achievable. The results (Fig. 4.12) revealed that both onset and peak temperatures of the $CaCO_3$ decomposition reaction increased as the heating rate increased. The temperature of the exothermic peak also increased as heating rate increased, however to a lesser extent. In the case of the 50°C/min, there is no plateau between the endothermic peak and the exothermic peak as those are observed in the DTA curves for heating rates of 5°C/min, 10°C/min, and 20°C/min, indicating that the decomposition of $CaCO_3$ (endothermic) partially overlaps with the reaction of calcium aluminate formation.

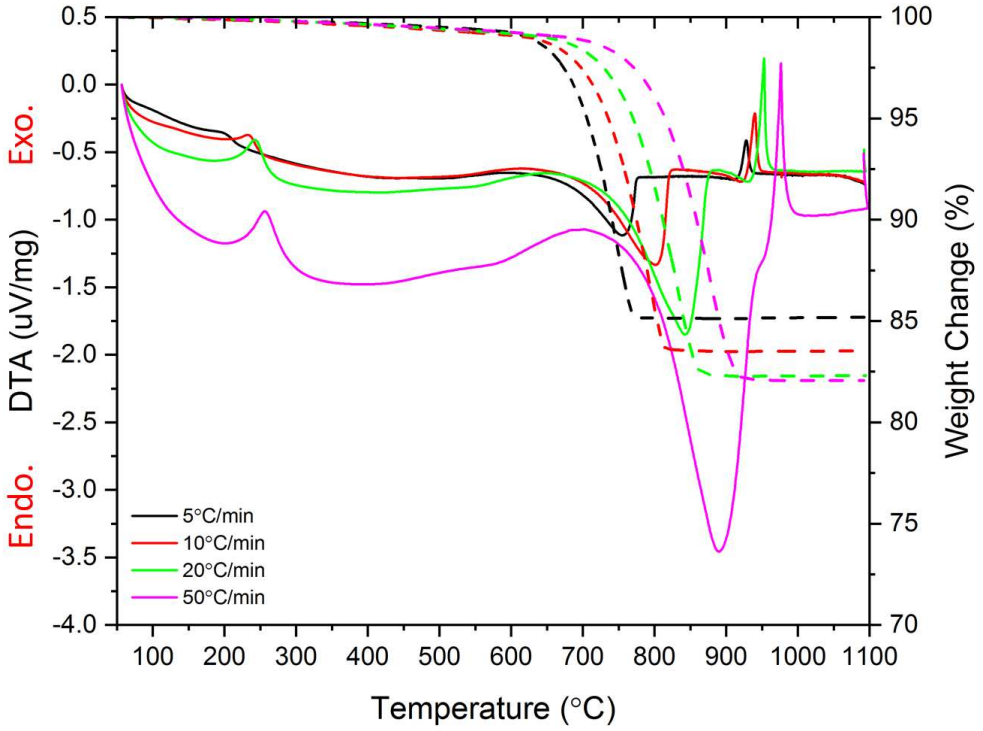

Figure 4.12: TG/DTA plots of 10Hr. BM powder tested using various heating rates

To test if a lower heating rate to reach the peak temperature of calcium aluminate formation (~ 900°C) in SPS would facilitate the decomposition of $CaCO_3$ prior to calcium aluminate formation, a sample was sintered using a 100°C/min heating rate to 800°C, followed by a 10°C/min ramp to 900°C, and then a final 100°C/min ramp to 1200°C. The SPS vacuum pressure change (Fig. 4.13) suggested that the modification in heating rate in such a narrow temperature range (800-900 °C) had a minimal effect on lowering the decomposition temperature of $CaCO_3$ in SPS.

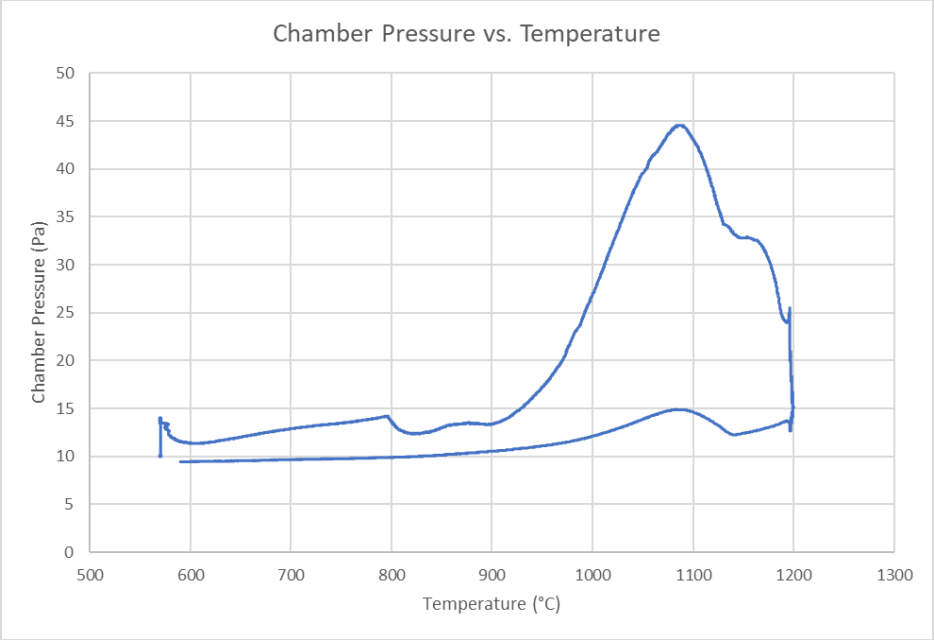

Figure 4.13: SPS chamber pressure vs. temperature for an *in-situ* sample sintered with a 10°C/min heating rate between 800°C and 900°C

4.3 Effect of Addition of Reinforcing Phases

The compositing approach, i.e., adding conductive phases in the precursor, discussed in CH. 3, was investigated for *in-situ* reaction sintering as well. One of the goals was to study if different additives could facilitate the decomposition of $CaCO_3$ prior to the initiation of calcium aluminate formation. One hypothesis was that a conductive pathway throughout the insulative powder compact could provide uniform heating throughout the sample during sintering, promoting the decomposition of $CaCO_3$ throughout the bulk of the sample. In addition, these additives provide a reducing environment inside the C12A7 precursor compact. For a direct comparison, C12A7 composite samples were sintered via *in-situ* reaction using the same weight percentages of CB, and Ti that were discussed in CH. 3. From the plots of SPS chamber pressure vs. temperature shown in Figure 4.14, the addition of Ti enabled the decomposition of $CaCO_3$ at lower temperatures, while the addition of CB had virtually no effect on the decomposition reaction.

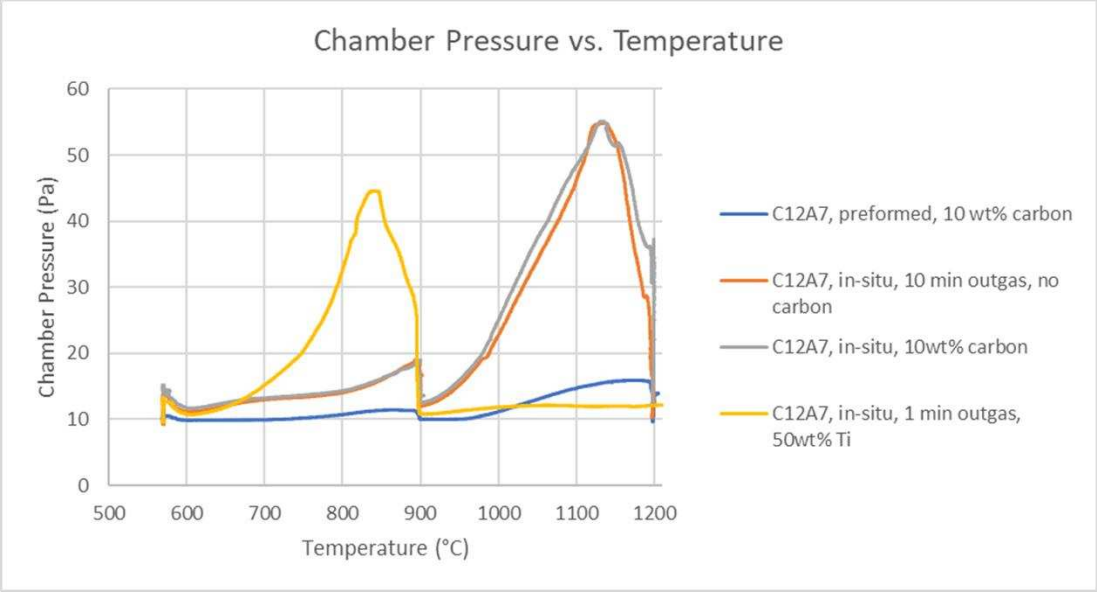

Figure 4.14: Chamber pressure vs. temperature for preformed and *in-situ* C12A7 in the presence of different additives

The fact that the addition of CB had no effect on the decomposition reaction implies that heat transfer through the powder compact is not the limiting factor of this reaction. The reduction in decomposition temperature via the addition of Ti may be explained in the context of an equilibrium existing between $CaCO_3$ and $CaO+CO_2$.

The equilibrium of

$$CaO_{(s)}+CO_{2(g)}=CaCO_3 \qquad \text{Equation 4.5}$$

occurs when the molar Gibbs free energies, G°, of each phase follow the equation below:

$$G°_{CaO(s)}+G°_{CO2(g)}+RT\ln(p_{CO_2(eq.T)})=G°_{CaCO3(s)} \qquad \text{Equation 4.6}$$

which is simplified to

$$\Delta G°=RT\ln p_{CO2(eq.T)} \qquad \text{Equation 4.7}$$

For the $CaCO_3$ system, $\Delta G°$ is given as[49]

$$\Delta G°=-168{,}400+144T \text{ joules} \qquad \text{Equation 4.8}$$

Eqns. 4.7 and 4.8 may be used to construct a plot of the equilibrium partial pressure of CO_2 with respect to temperature, as shown in Figure 4.15. While p_{CO2} in Earth's atmosphere is small (p_{CO2}=0.0039 atm),[1] this pressure is not exceeded in $CaCO_3$ until 550°C, at which point decomposition initiates. While $CaCO_3$ decomposition initiates at 550°C in air, the partial pressure of CO_2 must exceed the ambient partial pressure significantly for the decomposition to occur at a reasonable rate. Khinast et al. found that at 780°C, an increase in p_{CO2} from 0% to 5%, caused the time for complete $CaCO_3$ decomposition to be extended by an order of magnitude.[61]

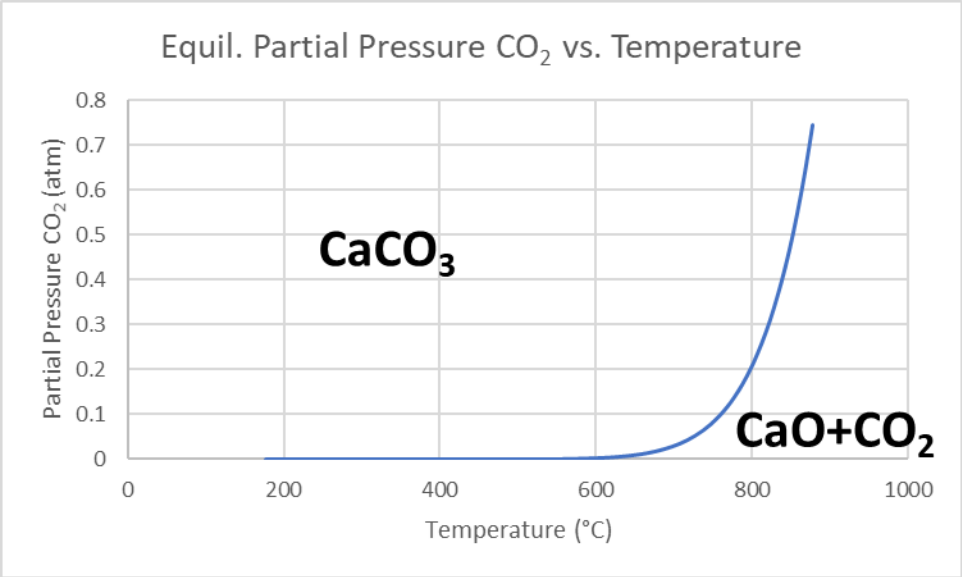

Figure 4.15: Equilibrium partial pressure of CO_2 vs. temperature

As a high carbon environment leads to an increase of p_{CO2}, and an increase of p_{CO2} leads to an increase in the decomposition temperature of $CaCO_3$, it is reasonable to assume that the decomposition temperature of $CaCO_3$ in SPS is far higher than the standard value reported in literature, as the $CaCO_3$ powder is surrounded by carbon. This also explains why the addition of CB particles to the powder compact had virtually no effect on the decomposition of $CaCO_3$.

The facilitation of $CaCO_3$ decomposition in SPS by Ti will be discussed based on the Ellingham diagram (Fig. 4.16).[49] The Ellingham diagram is constructed by plotting $\Delta G°$ versus T

for various oxidation reactions and normalizing per mole of O_2 involved in each reaction. Two reactions are involved in the oxidation of C:

$$C+O_2=CO_2 \qquad \text{Equation 4.9}$$

$$2C+O_2=2CO \qquad \text{Equation 4.10}$$

While the addition of C would have no effect on the decomposition/reduction of CO_2, it is seen in Figure 4.16 that Ti will reduce all carbon oxides below 1500°C. An additional feature of the Ellingham diagram is the nomographic plot of p_{o2} versus T, which provides the O_2 equilibrium partial pressure of any oxidation reaction at a given temperature, meaning that O_2 will be consumed by the oxidation reaction until the surrounding equilibrium O_2 partial pressure is established. It is seen in Figure 4.16 that the magnitude of ΔG for the oxidation of Ti is greater than the oxidation of C by a large margin. It is also seen that the equilibrium partial pressure of O_2 created by the oxidation of Ti is several orders of magnitude lower than that caused by the oxidation of C. It may be concluded that Ti is effectively reducing $CaCO_3$, leading to a reduction in the observed decomposition temperature.

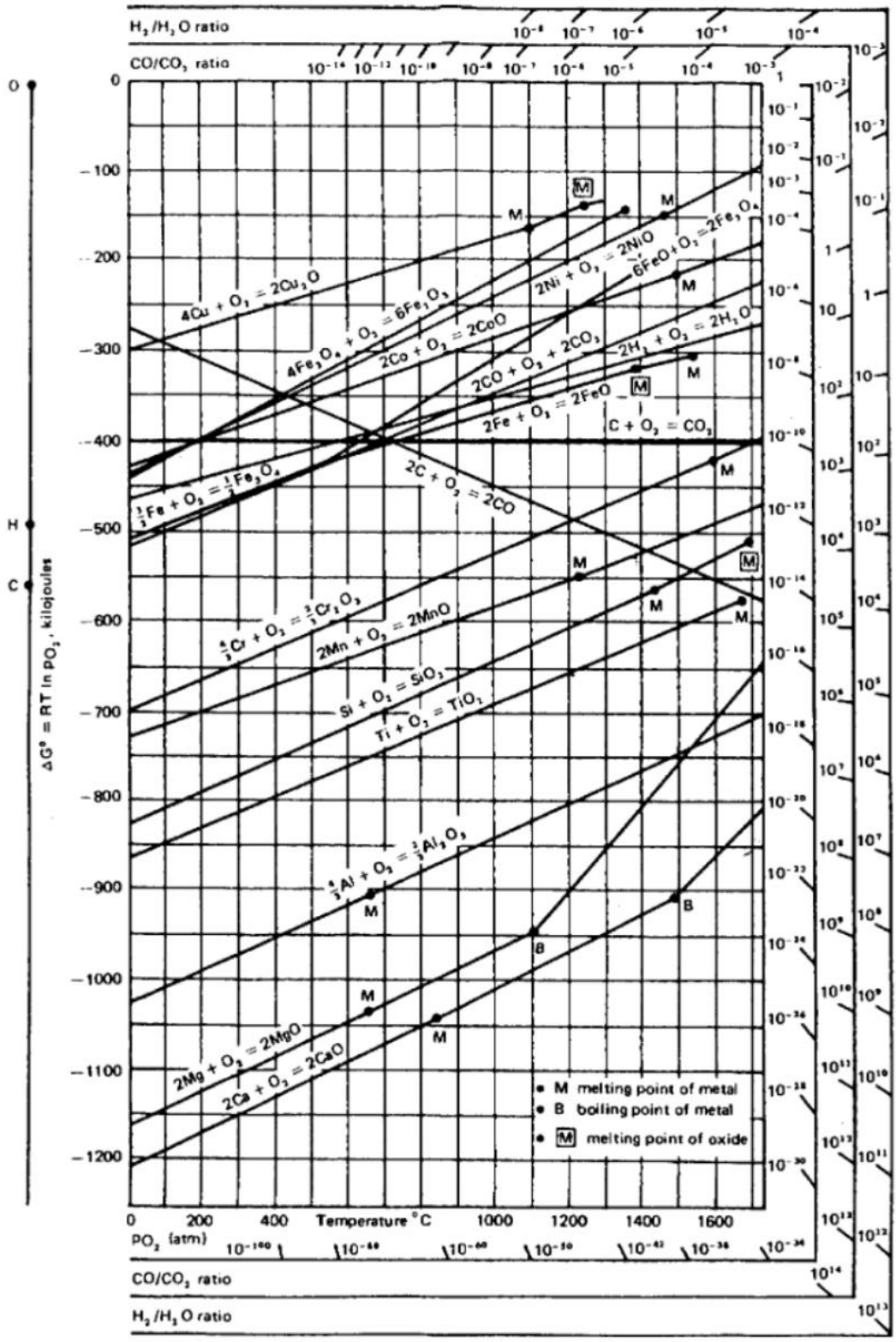

Figure 4.16: Ellingham diagram showing nomographic scale of P_{O2}[49]

The *in-situ*-Ti composite sample (C12A7-R5) and its' XRD pattern are shown in Figure 4.17. While Ti has been oxidized to TiO, and has further reacted with CaO to form $CaTiO_3$, the sample primarily displays C12A7.

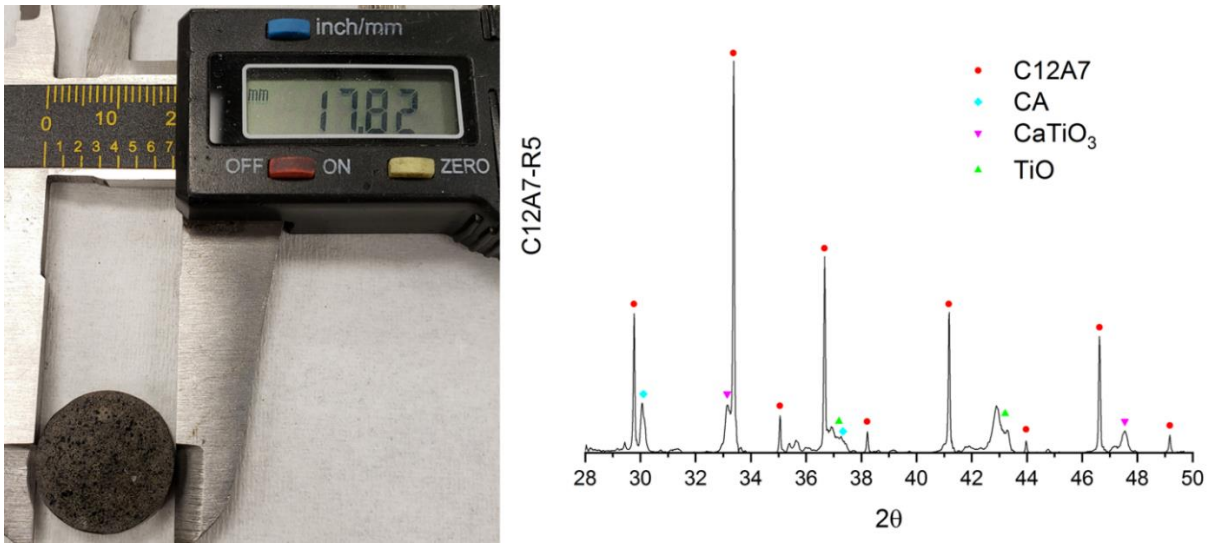

Figure 4.17: C12A7-R5 a) optical image b) XRD pattern

Figure 4.18 shows the results of EDS point mapping at a C12A7:e^--Ti interface. It is seen that the Ti region (point A) consists of TiO, indicating that appreciable oxidation of Ti has occurred. Between C12A7:e^- (point D) and the Ti region, a layer of $CaTiO_3$ (point B) has developed. As CaO was consumed to produce $CaTiO_3$, the resulting excess Al_2O_3 led to the formation of CA near this interface, as seen in the small, light phases within C12A7:e^- (point C).

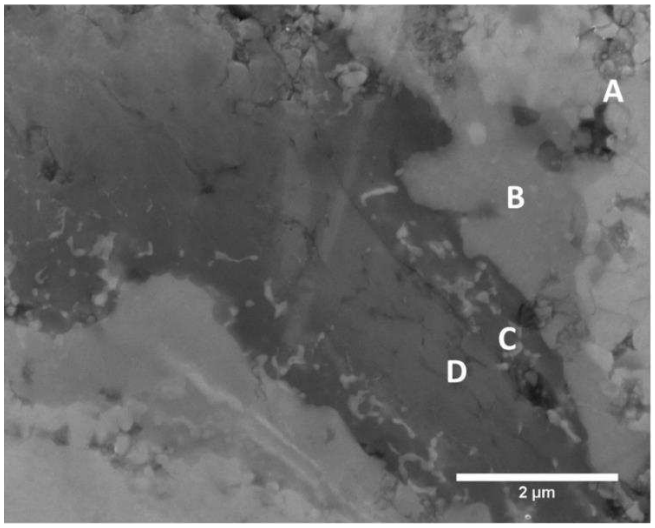

A: TiO

Element	At%
Ca	1.6
Al	0
O	52.7
Ti	45.0

B: $CaTiO_3$

Element	At%
Ca	16.6
Al	4.9
O	60.8
Ti	17.7

C: CA

Element	At%
Ca	13.0
Al	21.8
O	56.6
Ti	8.6

D: $C12A7:e^-$

Element	At%
Ca	20.2
Al	23.8
O	55.8
Ti	0.2

Figure 4.18: SEM image of $C12A7:e^-$-Ti interface showing the formation of a $CaTiO_3$ layer between the two phases

4.4 Discussion

Increased ball milling time was found to reduce the $CaCO_3$ particle size, which led to more efficient powder packing, as well as increased interfacial area between $CaCO_3$ and Al_2O_3. The effect of extended ball milling time on powder packing is seen in the decrease in porosity of sintered samples with respect to extended milling times. Increased interfacial area between $CaCO_3$ and Al_2O_3 facilitated the calcium aluminate formation reaction, as was observed in TG/DTA. Calcium aluminate formation was also found to initiate around 930°C. This observed formation temperature was pertinent to the *in-situ* formation of C12A7 in SPS, as complete decomposition of $CaCO_3$ was typically not achieved until 1100°C. The presence of CO_2 during calcium aluminate formation led to the formation of large pores that compromised the mechanical strength of the sintered samples or led to the formation of a soda-aluminate phase depending on the length scale of the pore network.

The effects of rapid heating rates on $CaCO_3$ decomposition and calcium aluminate formation were investigated via TG/DTA, and it was discovered that the high heating rates in SPS (100°C/min) were possibly increasing the $CaCO_3$ decomposition temperature such that decomposition was occurring during or after calcium aluminate formation. The use of a 10°C/min between 800°C and 900°C had minimal effect on $CaCO_3$ decomposition in SPS.

The C environment of SPS was found to increase the thermal stability of $CaCO_3$. The addition of a reducing phase (Ti) was found to suppress the $CaCO_3$ decomposition temperature such that complete decomposition occurred below 900°C. While the resulting TiO reacted with CaO to form a small interfacial layer of $CaTiO_3$, the composite sample was comprised primarily of C12A7:e^-.

Chapter 5 Processing and Characterization Work

In addition to fundamental investigation into the phase formation during the consolidation of mayenite (C12A7) and its precursor in SPS, special graphite tooling and machining processes were developed to make mayenite electride (C12A7:e^-)-composites with complex geometries. This chapter discusses the solutions to overcome the challenges of machining brittle materials while maintaining the properties of interest. In addition, the electronic properties of select samples were investigated by different characterization methods, including Kelvin probe force microscopy (KPFM), thermionic emission testing, and electron paramagnetic resonance (EPR). The combination of these techniques will provide quantitative information on the electronic characteristics of the electride materials.

5.1 Hemispheres: Consolidation and Post-Processing

C12A7:e^--Ti and C12A7:e^--TiB_2 composite samples with hemispherical geometry were required for thermionic emission testing. A stem part or a separate fixture with a 4-40 size threaded hole at least 5mm tall was also needed to fit the sample into the testing apparatus. The connection between the sample and the threaded rod should maintain ohmic contact, mechanical stability at high temperatures, and be inert relative to the sample and the threaded rod in the testing device. To consolidate these hemispheres, special graphite tooling was designed and manufactured via computer numerically controlled (CNC) machining. As shown in Figure 5.1, the tooling consists of a lower punch which provides the hemisphere shape, and an upper punch which provides a stem to the flat face of the hemisphere. Due to the self-contained crucible shape of this tooling, high

sintering temperatures, 1300°C and above, could be used without the concern of partial melting of the precursor or material escaping into the SPS vacuum chamber.

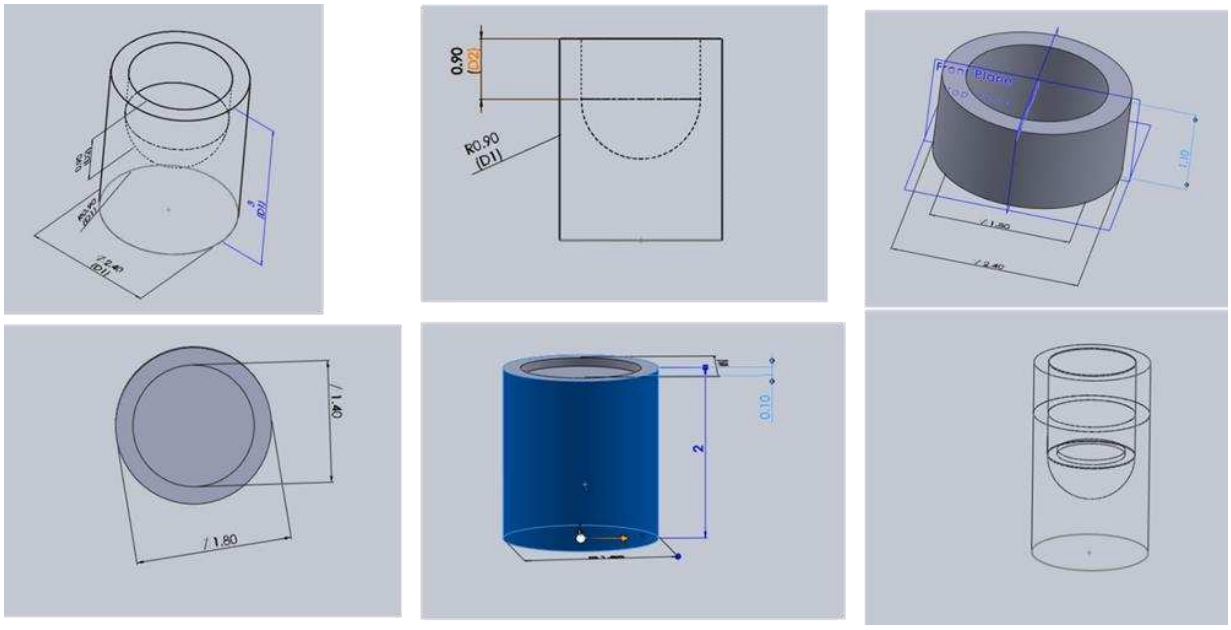

Figure 5.1: CAD images of hemisphere tooling showing individual parts and final assembly

While this tooling successfully provides the hemisphere shape of the samples, it has a disadvantage of only one-time use. Samples can be removed from the tooling only by breaking the tooling and grinding away any excess graphite. Different post-sintering processes were investigated for two different composite materials, C12A7:e^--Ti and C12A7:e^--TiB_2, to ensure that the hemisphere samples can be securely mounted to the test fixture. In the case of the Ti system, a thin Ti tube was made via SPS, with a thin graphite rod inserted into the Ti powder before sintering to allow the tube to be tapped to subsequently make a 4-40 threaded hole. The Ti tube is cut to the desired length, tapped, and then diffusion bonded onto the back of the hemisphere via the SPS. After the diffusion bonding, excess material was ground away, and the hole was re-tapped (Fig. 5.2). This post-sintering process route provides secure mounting of the sample to the test fixture, as well as a conductive connection to let current flow through the testing circuit.

Figure 5.2: Hemisphere with Ti mounting piece attached

The method for post processing C12A7:e^--Ti hemisphere samples is not viable for the C12A7:e^--TiB_2 system as Ti does not diffusion bond with TiB_2 readily due to the oxide layers that develop on the surface of each. No material was successfully identified in literature to provide sufficient diffusion bonding to the hemispheres without changing the 12:7 stoichiometric chemical composition of C12A7while still providing ohmic contact, thermal and mechanical stability. Therefore, an alternative approach was developed to make the threaded hole in the hemisphere itself. To accomplish this, the hemispheres were mounted into a modified lower hemisphere punch and secured with crystal bond. Once the hemispheres were secured, a diamond-coated coring bit was used to remove a core from the back of the hemisphere. A small graphite rod was then turned down to have a diameter slightly larger (approx. 0.005") than the hole in the back of the hemisphere. This small graphite rod was press-fit into the back of the hemisphere, and then ground to make a flat surface of the back of the hemisphere. Subsequently, the graphite rod was drilled and tapped to fit the threaded rod. If the graphite rod cannot be removed from the hemisphere by tugging on the threaded rod, the connection was considered mechanically secure. Ohmic contact is verified by measuring the electrical resistance, which should be low (<1Ω), between the hemisphere surface and the threaded rod. Extreme care is needed for every step in this process due

to the brittle nature of C12A7. The whole process route is shown schematically in Figure 5.3. The machining process developed for the TiB_2 system is also valid for the C12A7:e^--CB composite.

Figure 5.3: Schematic of procedure to add graphite mounting piece to hemispheres

5.2 Electronic Characterization Methods

KPFM, thermionic emission testing, and EPR were used to characterize the electronic properties of select sintered samples. The microstructure of a sample post-thermionic emission

testing was evaluated via SEM/EDS mapping. Due to their non-destructive natures, microstructures of samples post-KPFM and EPR were not evaluated.

5.2.1 Kelvin Probe Force Microscopy

KPFM is an atomic force microscopy (AFM)-based approach for determining the electronic properties of surfaces with high spatial resolution, on the order of nanometers.[43] KPFM operates by first scanning across the surface of a material with an AFM probe. Once the surface topology has been determined, the probe is raised and maintained at a set height above the sample surface. A contact potential difference develops between the probe tip and the sample surface due to their different work functions. If the tip and the sample are electrically connected, the contact potential difference will lead to the development of an electrostatic force, which causes the probe to deflect. This force is nullified by applying a bias to either the tip or the sample, the magnitude of which is equal to the contact potential difference.[43] KPFM was used to measure the spatial variation of the work function across the surface of a C12A7:e^--Ti composite. Testing was performed over both C12A7:e^- and Ti surfaces in ambient atmosphere at room temperature.

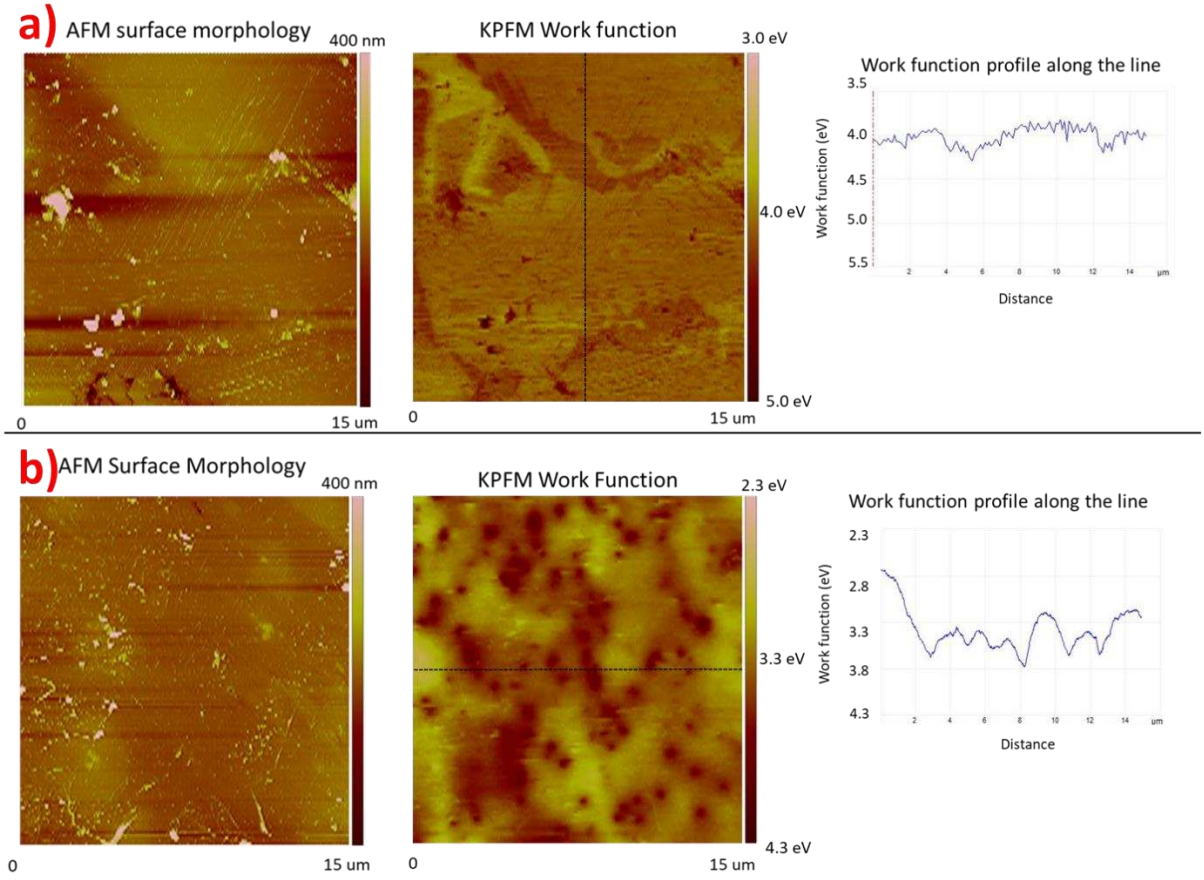

Figure 5.4: AFM and KPFM across C12A7:e$^-$-Ti composite a) Ti region b) C12A7:e$^-$ region

The surface morphology of the Ti region, shown in Figure 5.4a, reveals several submicron pores, as well as minor artifacts from mechanical polishing of the sample. It may be assumed that the white regions are pores due to the high negative value of roughness, as well as their corresponding high work functions. KPFM shows that the work function across the Ti region varies between 4 and 4.3 eV. The theoretical work function of Ti is 4.33 eV.[63] Variations in the work function of the Ti surface may be attributed to the presence of any impurities such as O or Al as discussed in CH. 3.[64]

AFM across the surface of the C12A7:e^- region, shown in Figure 5.4b, reveals that the surface contains several submicron pores, as well as artifacts from mechanical polishing, similar to the Ti region described above. KPFM shows that the work function of the C12A7:e^- region varies between 2.3 and 3.8 eV. The commonly accepted work function of C12A7:e^- is 2.1 eV.[13] Several high work function regions have nucleated throughout the C12A7:e^- region. As discussed in CH. 3, these may be regions where C3A has nucleated as there is a tendency for surrounding Ti particles to leach Al_2O_3 during SPS, resulting in the formation of C3A in the calcium aluminate region. The work function of C3A has not been reported in literature due to the lack of interest in its' electronic properties. This is the first documented use of KPFM for characterizing C12A7:e^-.

5.2.2 Thermionic Emission Testing

Thermionic emission testing is used to directly measure the emission current of a material as a function of temperature and voltage and may be used to calculate the work function of a material by Richardson's law.[3] This law may be given as:

$$J = A_G T^2 e^{-\frac{(\Phi)}{kT}} \quad (1)$$

where J is emission current density, A_g is Richardson's constant, T is the absolute temperature, Φ is the work function in eV, and k is Boltzmann's constant. In a typical experimental setup, the sample is placed in a vacuum chamber and exposed to a plasma. Measurements may be made under isoelectric or isothermal conditions, as a function of the other parameter. Thermionic emission testing was performed isothermally with varying voltage for a C12A7:e^--Ti composite. The maximum observed emission current was 5.5 mA at 500V and 1200°C. A work function of approximately 2.6eV was extracted from this measurement. The Schottky Plot is shown in Figure 5.5.

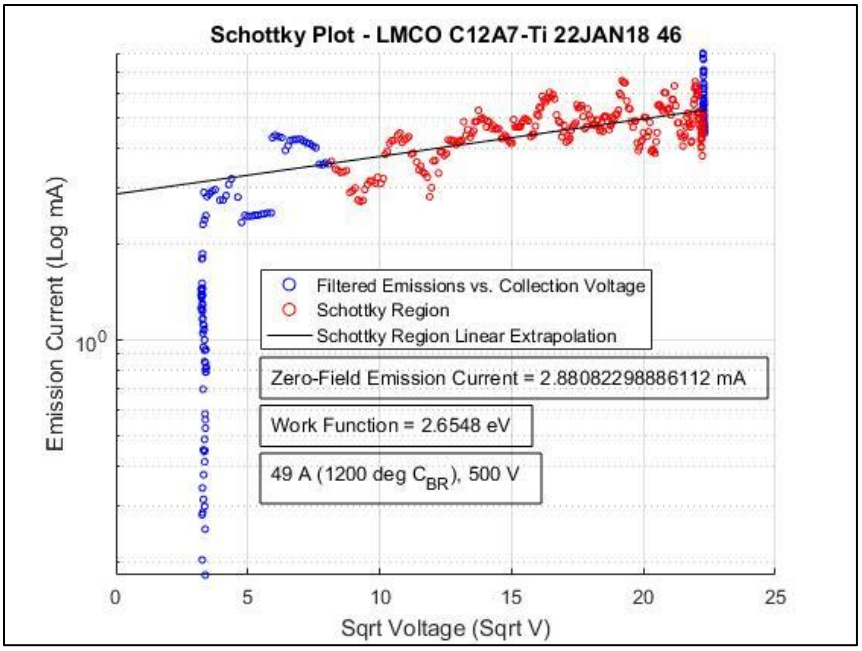

Figure 5.5: Schottky plot of emission current vs. voltage$^{1/2}$ of C12A7:e$^-$-Ti composite at 1200°C (Courtesy of The CEPPE Lab)

The microstructure of the sample was characterized after thermionic emission testing via SEM/EDS to observe whether any decomposition of the sample had occurred. It could not be determined if the C12A7:e$^-$ had decomposed as a layer of TiO_x had developed across the sample surface, as seen in Figure 5.6. In addition to this layer, Ta from the sample holder had been transferred onto the sample surface. If testing had been performed for a longer time, this layer would have developed into an insulative layer of TiO_2 and stymied further emission. This indicates that testing of C12A7:e$^-$-Ti composites at elevated temperatures must be performed in virtually O_2-free environments to ensure a long lifetime.

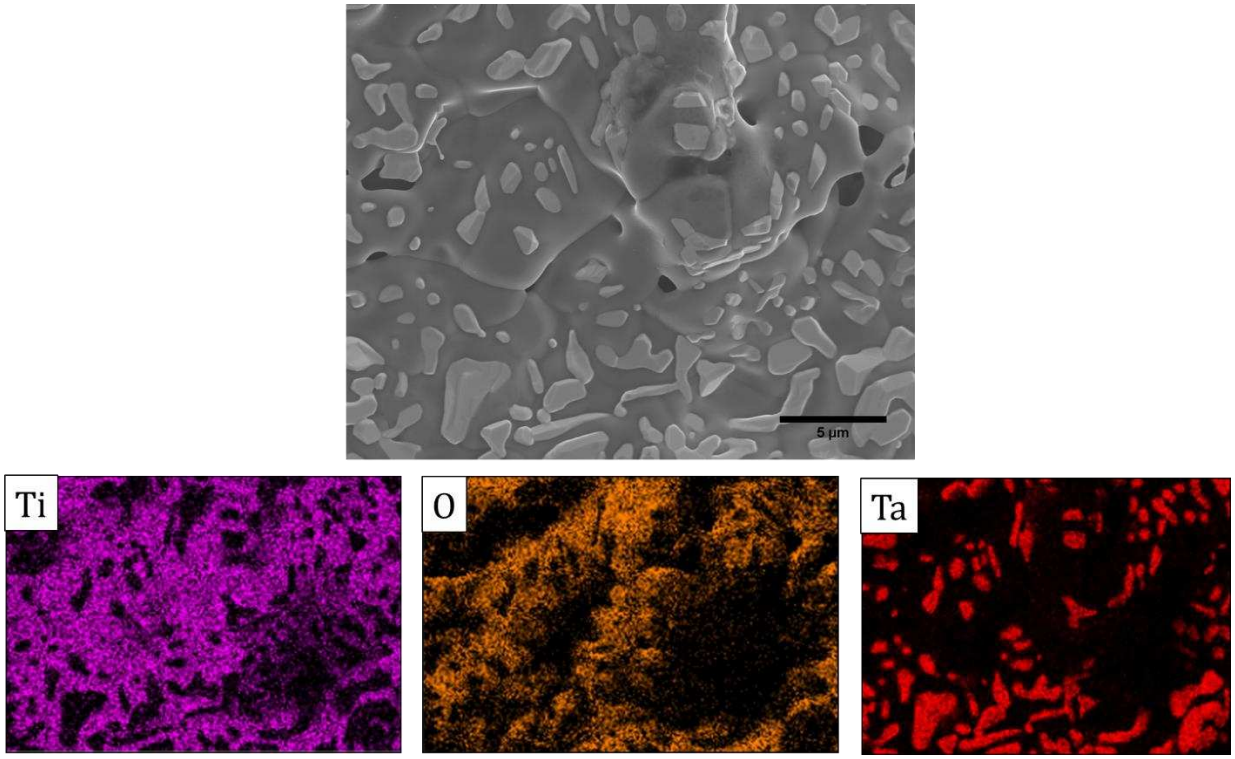

Figure 5.6: SEM and EDS mapping of C12A7:e$^-$-Ti composite surface post-thermionic emission testing

5.2.3 Electron Paramagnetic Resonance

The electronic behavior of C12A7:e$^-$, including electron transport and emission, is dependent on the electron concentration in the material. When the electron concentration reaches a critical point, $1x10^{21}/cm^3$, C12A7:e$^-$ displays metallic conduction.[50] Below this critical concentration, C12A7:e$^-$ behaves like a semiconductor. To evaluate the electron concentration of the C12A7:e$^-$ composites in this study, EPR was used. EPR is a technique which detects changes in the microwave absorption properties of materials with respect to a varying magnetic field. EPR measures the quantity of unpaired charge carriers in a material.[65] This technique has been widely applied in the studies of C12A7:e$^-$ with electron concentrations up to $5x10^{19}/cm^3$, at which point measurements from this technique saturate.[8] This detection saturation limit arises from the geometry of the cage structure, as well as the distribution of the electrons within the cages. Above

the saturation limit, there is a high probability that free electrons exist in neighboring cages, which form diamagnetic pairs and do not contribute to the EPR signal.

Based on the color of the sintered samples (CH. 3), C12A7-Foil and C12A7-C were selected for EPR characterization. C12A7-Foil was selected due to the dark coloration throughout the sample, indicating high electron density. C12A7-C was selected as the gray coloration of the C12A7 phases indicated that it had a low/intermediate electron density. Tests were performed using different orientations in the resonator cavity as well as using different microwave powers to verify that artifacts from these parameters could be identified. A representative spectrum of C12A7-Foil is shown in Figure 5.7a. The observed asymmetric, or Dysonian, line shape indicates that metallic conduction is observed in the sample. The signal generated from C12A7-C (Fig. 5.7b) is far weaker and displays a more Gaussian line shape, indicating that electron motion in C12A7-C is accomplished through a variable-range hopping method, like a semiconductor.[50] In the case of immobile free electrons in materials, such as F^+ centers, the EPR signal displays a Gaussian line shape.[66] Conductive materials i.e. metals display asymmetric Dysonian signals. These Dysonian signals are typically characterized by the asymmetry parameter A/B, which is the ratio of the upper to lower peak amplitudes.

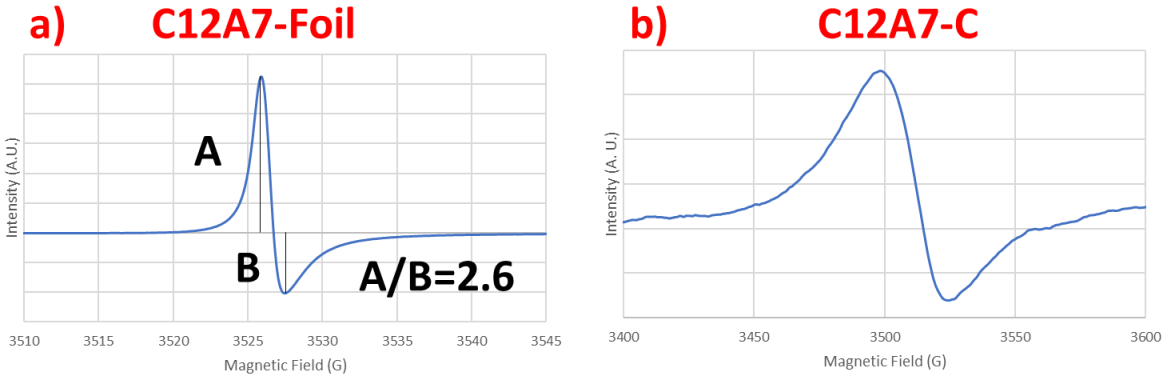

Figure 5.7: EPR spectrum generated by a) C12A7-Foil b) C12A7-C

A similar study performed by Matsuishi obtained a Dysonian EPR signal with an A/B ratio of 2.6 for single crystal C12A7:e^- which had been reduced by Ca shot at 700°C for 240 hours. While quantitative EPR yielded an electron density of $5x10^{19}/cm^3$, optical absorption provided an electron density of $2x10^{21}/cm^3$, which is just under the theoretical maximum of $2.33x10^{21}/cm^3$.[8] Therefore, while a quantitative value of the electron concentration of C12A7-Foil cannot be obtained through EPR, comparison with the literature leads to the conclusion that the electron concentration must lie in the area of $2x10^{21}/cm^3$. This treatment of a Dysonian EPR signal in C12A7:e^- has been applied elsewhere.[39]

Chapter 6 Conclusions and Vision of Future Work

Mayenite electride ($C12A7:e^-$) has emerged as a possible low-cost material for thermionic emission devices and other applications such as electro-catalysts and conductive oxides because of the abundant natural resource of its precursor materials. Despite extensive studies on the fundamental properties of $C12A7:e^-$ in the last decade, large knowledge gaps still exist in the field, especially the effect of formation of other calcium aluminate phases during the fabrication of bulk $C12A7:e^-$. In addition, electride composites were rarely investigated, which is a very important approach to form continuous ohmic contact through the electride materials for practical applications. This research addressed both practical issues and fundamental questions that remained in the field of C12A7 and $C12A7:e^-$ materials. This study proposed and investigated a novel *in-situ* reaction processing approach in SPS to fabricate bulk $C12A7:e^-$ and its composites, with a comparison to an alternative route where preformed C12A7 powder with different additives was used as feedstock material in SPS. The phase formation sequence accompanying the processing was investigated to reveal the effect of the select additives, including carbon black (CB), Ti, and TiB_2, on the formation of $C12A7:e^-$. Functional $C12A7:e^-$ composites with complex geometries were manufactured for thermionic emission testing. The electronic properties of select samples were characterized. This research has advanced the knowledge of processing $C12A7:e^-$ by identifying various phases that may form during the processing and when different reinforcing particles are added in the precursor to form composite materials, as well as by identifying key parameters that may be used to design and improve future manufacturing processes. This chapter will summarize the key findings of this work. Possible directions for future work are also discussed.

6.1 Preformed C12A7 Study

The formation of percolated C12A7:e^- composites by consolidating C12A7 with various additives was achieved. The effectiveness of each additive was assessed by considering the ability of each additive to reduce C12A7 while minimizing C12A7 decomposition. While Ti and TiB_2 appeared to have reduced C12A7 more effectively than CB, they also lead to the formation of secondary calcium aluminate phases, e.g., CA and C3A. The addition of Ti led to the formation of C3A and Ti_2Al intermetallic phase. The addition of TiB_2 led to the formation of CA, and the vaporization of B_2O_3•CaO. The use of Ti-foil above and below the C12A7 powder compact did not lead to any noticeable decomposition of C12A7 and produced C12A7:e^- with an electron concentration on the order of $10^{21}/cm^3$.

Percolation occurred in all of the particulate-reinforced composites, despite relatively low volume fractions of CB and TiB_2 added to the system compared to that of Ti. This may be attributed to the large discrepancy in particle size between C12A7 and the reinforcing phases, resulting from insufficient particle size reduction by hand-grinding of preformed C12A7 after heat-treatment. Phase segregation may also have occurred as the powders were hand blended. One future area of interest may lie in ball milling the compositing materials with C12A7 to obtain a more homogeneous mixture, both in terms of particle size distribution and in phase homogeneity. A continuous ohmic contact was successfully achieved in all the composite samples, verified by measurable conductivity values using a multimeter. Microstructure at C12A7:e^--additive interface was characterized to identify any possible interactions between the C12A7:e^- and the reinforcement particles. It was observed that when CB was added, C diffused into C12A7:e^-, which indicated the occurrence of the reduction reaction. With Ti as the additive, Al was leached from

C12A7:e^- and diffused into Ti, forming an insulative Ti-Al-O phase at the interface between the two constituents.

6.2 *In-Situ* C12A7 Study

Ball milling time has a significant effect on the formation of C12A7 and C12A7:e^- during SPS. Increased ball milling time led to a reduction of $CaCO_3$ particle size, as well as an increase in particle homogeneity. These changes in the precursor powder lead to increased interfacial area between $CaCO_3$ and Al_2O_3, which accelerates precursor consumption during the calcium aluminate formation reaction, as verified by TG/DTA and XRD. Reduction of $CaCO_3$ particle size also leads to a reduction of porosity in the sintered samples. Mass transport of the *in-situ* system during SPS is dominated by the diffusion of CaO into Al_2O_3 as opposed to the reduction of surface area which drives traditional sintering. Therefore, when the $CaCO_3$ particles are significantly larger than the Al_2O_3 particles, the Al_2O_3 particles essentially form a surface layer, and diffusion of CaO from the interior of the particle is obstructed.

The peak decomposition temperature of $CaCO_3$ observed in SPS (1090°C) is noticeably higher than the standard reported temperature reported in the literature, ~ 870°C.[62]Both fast heating rates in SPS and C-rich environment created by the graphite tooling increase the onset temperature of decomposition. This study revealed that the C-rich environment in SPS changed the chemical equilibrium between $CaCO_3$ and $CaO+CO_2$ and this chemical equilibrium effect is the predominant factor. The C-rich atmosphere established by the graphite tooling used in SPS increases the local CO_2 partial pressure, making $CaCO_3$ stable at higher temperatures. In addition, the presence of CO_2 lead to the formation of an insulative sodalite phase. The addition of Ti reduced CO_2 to C and O_2. Consequently, the $CaCO_3$ decomposition temperature is suppressed to a lower temperature than the case without Ti additions. The suppression of the $CaCO_3$

decomposition temperature is important to the *in-situ* formation of C12A7 in SPS as calcium aluminate formation initiates at approximately 930°C and the completion of $CaCO_3$ decomposition is required to form CaO prior to the formation of C12A7. The oxidation of Ti during this process can lead to the formation of $CaTiO_3$, and consequently a small amount of CA. Overall, the addition of Ti allowed for the successful *in-situ* formation of C12A7:e^- in SPS.

6.3 Manufacturing and Electronic Characterization

Hemispheres with stems on the flat face were successfully manufactured for both the C12A7:e^--Ti and C12A7:e^--TiB_2 systems. Methods to fasten the hemispheres to a test fixture such that ohmic contact was established between the hemisphere and the test fixture were developed for each system. While a viable post-sintering process method was identified to manufacture parts with complex geometries, some design features, such as a stem on the flat face of a hemisphere, necessitated the destruction of the tooling in order to remove the sample, making the manufacturing process expensive and time-consuming. Further effort needs to be explored to improve the graphite tooling design for complex geometries to save time and cost.

Various electronic characterization techniques were applied throughout this study. Kelvin probe force microscopy (KPFM) was used to map the work function variance of a C12A7:e^--Ti composite across its surface. KPFM results allow us to correlate local electronic properties with sample microstructure. We found Ti regions exhibit an average work function of 4 eV and the C12A7:e- region exhibit an average work function of 2.8 eV±0.4 eV, with fluctuations due to the presence of other calcium aluminate phases. In contrast, thermionic emission testing provided the overall work-function of the select C12A7:e^--Ti sample as approximately 2.6 eV. Characterization of the post-testing sample revealed that a TiO_x layer grew across the sample surface would have eventually prevented further electron emission. This type of testing should ideally be performed

in ultralow O_2 environments to accurately determine steady-state electron emission behavior. EPR was used to estimate the electron concentration of a monolithic C12A7:e^- sample that had been reduced by Ti foil. While the crystal structure of C12A7:e^- does not allow for accurate electron density quantitation above a certain electron concentration, the presence of a Dysonian line shape establishes that the clathrate electrons are conducting metallically. The asymmetry parameter A/B may be used to compare the electron concentration of C12A7:e^- formed here to that formed in other studies. This method may be used to determine the quality of C12A7:e^- powder formed in future studies.

6.4 Vision of future research work

Selection of additives to make electride composites

Cationic doping of C12A7 is a growing topic of research. The principle benefit of cationic doping, where Ca and Al cations in the framework of C12A7 are replaced by some other cations, is that an electron concentration higher than the current theoretical maximum of C12A7:e^- can be obtained when cations having a valence higher than the matrix cations are used as the dopants. As a majority of the candidates for cationic doping are metals, it may be possible to form a percolated, cation-doped C12A7:e^- composite by blending C12A7 or C12A7:e^- powders with one of the cationic dopants and then consolidating the powder compact via SPS, similar to the preformed C12A7 study described in this study.

The observed interactions between C12A7, its precursors, and the compositing materials used in this study may be used to identify other additives that may simultaneously form a percolating network as well as dope the surrounding C12A7 with cations. Potential candidates of metal additives for preformed C12A7 and the *in-situ* formation of C12A7 are discussed in this

section. An in-depth literature review of cation-doped C12A7 was performed by Salasin and Rawn. Initial candidates may be selected from Table 6.1. Rare-earth metals are excluded as the original intent of this work is to create functional electronic materials with elements that may be extracted in economically useful quantities. A table listing these elements, as well some basic properties of each, is shown in Table 6.1. Sr, Ga, Mg, and Cu may be eliminated from the list of potential compositing candidates due to their relatively low melting temperatures. Mg may additionally be eliminated as it will reduce Al_2O_3, which could lead to C12A7 decomposition.[49] Mn is eliminated as it may potentially form oxides that will melt during processing, similar to any MB_2 compounds. Some oxides of Mn are also highly volatile.[67]

Table 6.1: Cationic dopants as candidate compositing materials showing T_m and reduction potential[68]

Element	T_m(°C)	Reduction Ability
Sr	777	Will reduce Al_2O_3
Fe	1538	Weaker than C
Cu	1084	Weaker than C
Nb	2477	Appropriate
Ta	3017	Appropriate
Co	1495	Weaker than C
V	1910	Appropriate
Ni	1455	Weaker than C
Mg	650	Will reduce Al_2O_3
Mn	1246	Oxides melt, volatile
Ga	30	Appropriate

Red font in Table 6.1 indicates the reasons why the corresponding metals cannot be considered as an additive.

The effectiveness of each candidate material can be anticipated by inspecting the position of each on the Ellingham diagram. Fe, Cu, Co, and Ni all have an O_2 reduction potential lower than C, so while they may dope C12A7 and allow for the formation of a percolated composite, the time required to convert C12A7 to C12A7:e^- during SPS would be determined by the reaction of C12A7 with C. These elements would also not allow for the *in-situ* formation of C12A7 during SPS. Nb, Ta, and V all have reduction potentials that are intermediate between C and Al, indicating that they would not necessarily decompose C12A7, and that they would accelerate the C12A7:e^- conversion time. Like Ti, oxides of these elements will undergo carbothermal reduction in low pressure environments in temperature ranges between 1100°C-1200°C, which can be detrimental to thermionic emission depending on the extent of carbide formation. One oxide of V, V_2O_5, melts at 690°C, but formation of this oxide may be avoided by using appropriately higher quantities of V.

While oxide and carbide formation of each element may be estimated from literature review, it is difficult to predict the formation of intermetallic phases between reinforcing phases and Ca or Al. The presence of electric field effects in SPS also potentially has a great effect on the formation of intermetallic phases. Therefore, future work is needed to address these questions.

Microstructure Design

The surface of C12A7:e^- is a predominant factor that limits emission currents as work function is a surface property.[69] Therefore emission current density can be improved by increasing the specific surface area of a piece of C12A7:e^-. This may be accomplished by reducing the applied pressure during consolidation and reduction of C12A7:e^- in SPS to form a micro-porous surface

and in the bulk. While the formation of a porous body of C12A7:e^- would increase the specific surface area, the formation of pores in the bulk of the sample is undesirable when mechanical strength is also required. It was seen in CH. 4 that large pores within C12A7:e^- can lead to fracture while removing a sample from the SPS (C12A7-R1). It was also discussed in CH. 3 that pores are an insulative phase, so the presence of pores in the bulk of a sample would lead to a reduction in maximum electron density, as well as impede electron mobility. Given these facts, a desirable microstructure design is to have microporous surface for enhanced electron emission and a dense bulk interior. This may be achieved by sintering graded C12A7, with one bulk layer consisting of pure C12A7 and a thin (approx. 0.5 mm) surface layer of 90-10wt% C12A7-carbon black. The carbon black could subsequently be burnt out of the composite, leaving behind a porous surface. A final reduction step with Ti foil would yield C12A7:e^- with a porous emission surface.

References

(1) Lide, D. R.; Baysinger, G.; Chemistry, S.; Berger, L. I.; Goldberg, R. N.; Kehiaian, H. V. CRC Handbook of Chemistry and Physics. 2661.

(2) Neamen, D. A. *Semiconductor Physics and Devices*, 4th ed.; McGraw-Hill, 2011.

(3) Coggins, J. L.; Stickney, R. E. Adsorption Studies Based on Thermionic Emission Measurements: I. Cesium on Single-Crystal Tungsten. *Surface Science* **1968**, *11* (3), 355–369.

(4) Bakr, M.; Kawai, M.; Kii, T.; Ohgaki, H. CeB_6 : Emission Performance and Uniformity Compared With LaB_6 for Thermionic RF Guns. *IEEE Transactions on Electron Devices* **2016**, *63* (3), 1326–1332. https://doi.org/10.1109/TED.2016.2520951.

(5) Patnaik, P. *Handbook of Inorganic Chemicals*; McGraw-Hill handbooks; McGraw-Hill: New York, 2003.

(6) Dye, J. L. Electrides: From 1D Heisenberg Chains to 2D Pseudo-Metals. *Inorganic Chemistry* **1997**, *36* (18), 3816–3826.

(7) Jeevaratnam, J.; Glasser, F. P.; Dent Glasser, L. S. Anion Substitution and Structure of 12CaO•7Al2O3. *Journal of the American Ceramic Society* **1964**, *47* (2), 105.

(8) Matsuishi, S.; Toda, Y.; Miyakawa, M.; Hayashi, K.; Kamiya, T.; Hirano, M.; Tanaka, I.; Hosono, H. High-Density Electron Anions in a Nanoporous Single Crystal: $[Ca_{24}Al_{28}O_{64}]^{4+}(4e)^{-}$. *Science* **2003**, *301*, 5.

(9) Li, Q. X.; Hayashi, K.; Nishioka, M.; Kashiwagi, H.; Hirano, M.; Torimoto, Y.; Hosono, H.; Sadakata, M. Absolute Emission Current Density of O^- from $12CaO•7Al_2O_3$ Crystal. *Applied Physics Letters* **2002**, *80* (22), 4259–4261. https://doi.org/10.1063/1.1476958.

(10) Palacios, L.; Cabeza, A.; Bruque, S.; García-Granda, S.; Aranda, M. A. G. Structure and Electrons in Mayenite Electrides. *Inorganic Chemistry* **2008**, *47* (7), 2661–2667. https://doi.org/10.1021/ic7021193.

(11) Toda, Y.; Matsuishi, S.; Hayashi, K.; Ueda, K.; Kamiya, T.; Hirano, M.; Hosono, H. Field Emission of Electron Anions Clathrated in Subnanometer-Sized Cages in $[Ca_{24}Al_{28}O_{64}]^{4+}(4e^-)$. *Advanced Materials* **2004**, *16* (8), 685–689. https://doi.org/10.1002/adma.200306484.

(12) Kim, S. W.; Matsuishi, S.; Nomura, T.; Kubota, Y.; Takata, M.; Hayashi, K.; Kamiya, T.; Hirano, M.; Hosono, H. Metallic State in a Lime−Alumina Compound with Nanoporous Structure. *Nano Letters* **2007**, *7* (5), 1138–1143. https://doi.org/10.1021/nl062717b.

(13) Toda, Y.; Kim, S. W.; Hayashi, K.; Hirano, M.; Kamiya, T.; Hosono, H.; Haraguchi, T.; Yasuda, H. Intense Thermal Field Electron Emission from Room-Temperature Stable Electride. *Applied Physics Letters* **2005**, *87* (25), 254103. https://doi.org/10.1063/1.2149989.

(14) Hosono, H.; Kim, S. W.; Miyakawa, M.; Matsuishi, S.; Kamiya, T. Thin Film and Bulk Fabrication of Room-Temperature-Stable Electride C12A7:e^- Utilizing Reduced Amorphous $12CaO•7Al_2O_3$(C12A7). *Journal of Non-Crystalline Solids* **2008**, *354* (19–25), 2772–2776. https://doi.org/10.1016/j.jnoncrysol.2007.09.090.

(15) Toda, Y.; Kubota, Y.; Hirano, M.; Hirayama, H.; Hosono, H. Surface of Room-Temperature-Stable Electride $[Ca_{24}Al_{28}O_{64}]^{4+}(e^-)_4$: Preparation and Its Characterization by Atomic-Resolution Scanning Tunneling Microscopy. *ACS Nano* **2011**, *5* (3), 1907–1914. https://doi.org/10.1021/nn102839k.

(16) German, R. M. *Particulate Composites*; Springer Science+Business Media: New York, NY, 2016.
(17) Yoshizumi, T.; Hayashi, K. Thermionic Electron Emission from a Mayenite Electride–Metallic Titanium Composite Cathode. *Applied Physics Express* **2013**, *6* (1), 015802. https://doi.org/10.7567/APEX.6.015802.
(18) Teusner, M.; De Souza, R. A.; Krause, H.; Ebbinghaus, S. G.; Martin, M. Oxygen Transport in Undoped and Doped Mayenite. *Solid State Ionics* **2016**, *284*, 25–27. https://doi.org/10.1016/j.ssi.2015.11.024.
(19) Miyakawa, M.; Hirano, M.; Kamiya, T.; Hosono, H. High Electron Doping to a Wide Band Gap Semiconductor $12CaO{\bullet}7Al_2O_3$ Thin Film. *Applied Physics Letters* **2007**, *90* (18), 182105. https://doi.org/10.1063/1.2735280.
(20) Boysen, H.; Lerch, M.; Stys, A.; Senyshyn, A. Structure and Oxygen Mobility in Mayenite ($Ca_{12}Al_{14}O_{33}$): A High-Temperature Neutron Powder Diffraction Study. *Acta Crystallographica Section B Structural Science* **2007**, *63* (5), 675–682. https://doi.org/10.1107/S0108768107030005.
(21) Calcium aluminates https://en.wikipedia.org/wiki/Calcium_aluminates (accessed Jun 9, 2019).
(22) Jiang, D.; Zhao, Z.; Mu, S.; Phaneuf, V.; Tong, J. Simple and Efficient Fabrication of Mayenite Electrides from a Solution-Derived Precursor. *Inorganic Chemistry* **2017**, *56* (19), 11702–11709. https://doi.org/10.1021/acs.inorgchem.7b01655.
(23) Tian, Y.; Pan, X.; Yu, H.; Tu, G. Formation Mechanism of Calcium Aluminate Compounds Based on High-Temperature Solid-State Reaction. *Journal of Alloys and Compounds* **2016**, *670*, 96–104. https://doi.org/10.1016/j.jallcom.2016.02.059.
(24) Salasin, J.; Rawn, C. In-Situ Kinetic Investigation of Calcium Aluminate Formation. *Ceramics* **2018**, *1* (1), 175–197. https://doi.org/10.3390/ceramics1010016.
(25) Khan, K.; Khan Tareen, A.; Elshahat, S.; Yadav, A.; Khan, U.; Yang, M.; Bibbò, L.; Ouyang, Z. Facile Synthesis of a Cationic-Doped $[Ca_{24}Al_{28}O_{64}]^{4+}(4e^-)$ Composite *via* a Rapid Citrate Sol–Gel Method. *Dalton Transactions* **2018**, *47* (11), 3819–3830. https://doi.org/10.1039/C7DT04543C.
(26) Suryanarayana, C. Mechanical Alloying and Milling. *Progress in Materials Science* **2001**, 184.
(27) Eufinger, J.-P.; Schmidt, A.; Lerch, M.; Janek, J. Novel Anion Conductors – Conductivity, Thermodynamic Stability and Hydration of Anion-Substituted Mayenite-Type Cage Compounds $C_{12}A_7$:X (X = O, OH, Cl, F, CN, S, N). *Phys. Chem. Chem. Phys.* **2015**, *17* (10), 6844–6857. https://doi.org/10.1039/C4CP05442C.
(28) Zou, W.; Khan, K.; Zhao, X.; Zhu, C.; Huang, J.; Li, J.; Yang, Y.; Song, W. Direct Fabrication of C12A7 Electride Target and Room Temperature Deposition of Thin Films with Low Work Function. *Materials Research Express* **2017**, *4* (3), 036408. https://doi.org/10.1088/2053-1591/aa63c7.
(29) Rudradawong, C.; Ruttanapun, C. High Temperature Electrical and Thermal Properties of Activated Bamboo Charcoal/C12A7 Mayenite Composite Prepared by Carbon Diffusion Process. *Materials Chemistry and Physics* **2019**, *226*, 296–301. https://doi.org/10.1016/j.matchemphys.2019.01.028.
(30) Singh, V. K.; Ali, M. M.; Mandal, U. K. Formation Kinetics of Calcium Aluminates. *Journal of the American Ceramic Society* **1990**, *73* (4), 872–876.

(31) German, R. M. Geometric Trajectories during Sintering. In *Sintering: from Empirical Observations to Scientific Principles*; Elsevier, 2014; pp 141–181. https://doi.org/10.1016/B978-0-12-401682-8.00006-9.
(32) Mackenzie, K. J. D.; Fletcher, R. A. The Formation of Portland Cement Clinker under Applied Electric Fields. I. Thermal Reaction Sequence and Kinetics of Clinker Phase Formation. *Thermochimica Acta* **1979**, *28* (1), 161–173.
(33) Franceschin, G.; Flores-Martínez, N.; Victorio, G. V.; Ammar, S.; Valenzuela, R. Sintering and Reactive Sintering by Spark Plasma Sintering (SPS). In *Sintering of Functional Materials*; Shishkovsky, I., Ed.; InTech, 2018. https://doi.org/10.5772/intechopen.68871.
(34) Baptista, M.; Kovalevsky, A. V.; Sarabando, A. R.; Ferro, M. C.; Capela, I.; Frade, J. R. Highly-Porous Mayenite-Based Ceramics by Combined Suspension Emulsification and Reactive Sintering. *Materials Letters* **2019**, *237*, 41–44. https://doi.org/10.1016/j.matlet.2018.11.061.
(35) Standard Systems for Research and Production http://fuji-sps.sakura.ne.jp/products/seisannyou/e_seisannyou.html (accessed Jun 9, 2019).
(36) Guillon, O.; Gonzalez-Julian, J.; Dargatz, B.; Kessel, T.; Schierning, G.; Räthel, J.; Herrmann, M. Field-Assisted Sintering Technology/Spark Plasma Sintering: Mechanisms, Materials, and Technology Developments: FAST/SPS: Mechanisms, Materials, and Technology Developments. *Advanced Engineering Materials* **2014**, *16* (7), 830–849. https://doi.org/10.1002/adem.201300409.
(37) Chung, J. H.; Ryu, J. H.; Eun, J. W.; Choi, B. G.; Shim, K. B. One-Step Synthesis of a 12CaO•7Al2O3 Electride via the Spark Plasma Sintering (SPS) Method. *Electrochemical and Solid-State Letters* **2011**, *14* (12), E41. https://doi.org/10.1149/2.021112esl.
(38) Li, F.; Zhang, X.; Liu, H.; Zhao, J.; Xiao, Y.; Feng, Q.; Zhang, J. Rapid Synthesis of Inorganic $[Ca_{24}Al_{28}O_{64}]^{4+}(e^{-})_4$ Electride and Its Performance as an Electron Thermal Emitter. *Vacuum* **2018**, *158*, 152–157. https://doi.org/10.1016/j.vacuum.2018.09.055.
(39) Li, F.; Zhang, X.; Liu, H.; Zhao, J.; Xiao, Y.; Feng, Q.; Zhang, J. In Situ Synthesis of $[Ca_{24}Al_{28}O_{64}]^{4+}(4e^{-})$ Electride Ceramic from C12A7 + C3A Mixture Precursor. *Journal of the American Ceramic Society* **2018**. https://doi.org/10.1111/jace.16103.
(40) Chou, K.-S. Formation of Calcium Aluminates in the Lime Sinter Process. **1979**.
(41) 4x1000ml Gear-Drive 4-Liter Planetary Ball Mill https://www.acrossinternational.com/4x1000ml-Gear-Drive-4-Liter-Planetary-Ball-Mill-PQN4.htm (accessed Jun 9, 2019).
(42) Blokhina, I. A.; Ivanov, V. V. Analysis of TiB_2 Powders Oxidation in the Air. *Journal of Thermal Analysis and Calorimetry* **2015**, *119* (1), 123–130. https://doi.org/10.1007/s10973-014-4196-2.
(43) Kalinin, S.; Gruverman, A. *Scanning Probe Microscopy*; Springer: New York, NY, 2007.
(44) McLachlan, D. S.; Blaszkiewicz, M.; Newnham, R. E. Electrical Resistivity of Composites. *Journal of the American Ceramic Society* **1990**, *73* (8), 2187–2203. https://doi.org/10.1111/j.1151-2916.1990.tb07576.x.
(45) Xie, Z. M.; Zhang, T.; Liu, R.; Fang, Q. F.; Miao, S.; Wang, X. P.; Liu, C. S. Grain Growth Behavior and Mechanical Properties of Zirconium Micro-Alloyed and Nano-Size Zirconium Carbide Dispersion Strengthened Tungsten Alloys. *International Journal of Refractory Metals and Hard Materials* **2015**, *51*, 180–187. https://doi.org/10.1016/j.ijrmhm.2015.03.019.

(46) Landauer, R. Electrical Conductivity in Inhomogeneous Media. In *AIP Conference Proceedings*; AIP, 1978; Vol. 40, pp 2–45. https://doi.org/10.1063/1.31150.
(47) Bhattacharya, S. K.; Chaklader, A. C. D. Review on Metal-Filled Plastics. Part 1. Electrical Conductivity. *Polym.-Plast. Technol. Eng.* **1982**, *19* (1), 21–51.
(48) Li, X. L.; Hillel, R. Reactions and Phase Relations in the Ti-Al-O System. *Acta metall. mater.* **1992**, *40* (11), 3149-3157.
(49) Gaskell, D. *Introduction to the Thermodynamics of Materials*, 5th ed.; Taylor and Francis: New York, 2008.
(50) Kim, S. W.; Hosono, H. Synthesis and Properties of $12CaO•7Al_2O_3$ Electride: Review of Single Crystal and Thin Film Growth. *Philosophical Magazine* **2012**, *92* (19–21), 2596–2628. https://doi.org/10.1080/14786435.2012.685770.
(51) Woo, Y.-C.; Kang, H.-J.; Kim, D. J. Formation of TiC Particle during Carbothermal Reduction of TiO_2. *Journal of the European Ceramic Society* **2007**, *27* (2–3), 719–722. https://doi.org/10.1016/j.jeurceramsoc.2006.04.090.
(52) Hayun, S.; Meir, S.; Kalabukhov, S.; Frage, N.; Zaretsky, E. Phase Constitution and Dynamic Properties of Spark Plasma-Sintered Alumina-Titanium Composites. *Journal of the American Ceramic Society* **2016**, *99* (2), 573–580. https://doi.org/10.1111/jace.13992.
(53) Orrú, R.; Cao, G.; Munir, Z. A. Field-Activated Combustion Synthesis of Titanium Aluminides. *Metallurgical and Materials Transactions A* **1999**, *30* (4), 1101–1108. https://doi.org/10.1007/s11661-999-0162-1.
(54) Schneider, S. J. *Compilation of the Melting Points of the Metal Oxides*; NBS MONO 68; National Bureau of Standards: Gaithersburg, MD, 1963. https://doi.org/10.6028/NBS.MONO.68.
(55) Jensen, M. S.; Einarsrud, M.-A.; Grande, T. The Effect of Surface Oxides During Hot Pressing of TiB_2. *Journal of the American Ceramic Society* **2009**, *92* (3), 623–630. https://doi.org/10.1111/j.1551-2916.2009.02923.x.
(56) Carlson, E. The System: $CaO-B_2O_3$. *Bureau of Standards Journal of Research* **1932**, *9*, 825–832.
(57) Grente, K.; Rebillat, F.; Langlais, F. Synthesis, Characterization and High Temperature Corrosion of Glass-Ceramics in the B_2O_3-Al_2O_3-SiO_2 System. In *High temperature corrosion and materials chemisty IV*; Paris, France, 2003.
(58) Ebbinghaus, S. G.; Krause, H.; Syrowatka, F. Floating Zone Growth of Large and Defect-Free $Ca_{12}Al_{14}O_{33}$ Single Crystals. *Crystal Growth & Design* **2013**, *13* (7), 2990–2994. https://doi.org/10.1021/cg400406t.
(59) Brenchley, M. E.; Weller, M. T. Synthesis and Structure of Sulfide Aluminate Sodalites. *Journal of Materials Chemistry* **1992**, *2* (10), 1003. https://doi.org/10.1039/jm9920201003.
(60) Muniz, F. T. L.; Miranda, M. A. R.; Morilla dos Santos, C.; Sasaki, J. M. The Scherrer Equation and the Dynamical Theory of X-Ray Diffraction. *Acta Crystallographica Section A Foundations and Advances* **2016**, *72* (3), 385–390. https://doi.org/10.1107/S205327331600365X.
(61) Khinast, J.; Krammer, G. F.; Brunner, Ch.; Staudinger, G. Decomposition of Limestone: The Influence of CO_2 and Particle Size on the Reaction Rate. *Chemical Engineering Science* **1996**, *51* (4), 623–634. https://doi.org/10.1016/0009-2509(95)00302-9.
(62) Kissinger, H. E. Reaction Kinetics in Differential Thermal Analysis. *Analytical Chemistry* **1957**, *29* (11), 1702–1706. https://doi.org/10.1021/ac60131a045.

(63) Skriver, H. L.; Rosengaard, N. M. Surface Energy and Work Function of Elemental Metals. *Physical Review B* **1992**, *46* (11), 7157–7168. https://doi.org/10.1103/PhysRevB.46.7157.
(64) Michaelson, H. B. The Work Function of the Elements and Its Periodicity. *J. Appl. Phys.* **1977**, *48* (11), 6.
(65) Eaton, G. R., Eaton, S. S., Barr, D. P., Weber, R. T. *Quantitative EPR*; Springer: Wien ; New York, 2010.
(66) Laguta, V.; Buryi, M.; Tkachenko, S.; Arhipov, P.; Gerasymov, I.; Sidletskiy, O.; Laguta, O.; Nikl, M. Oxygen-Vacancy Centers in Y3Al5O12 Garnet Crystals: Electron Paramagnetic Resonance and Dielectric Spectroscopy Study. 19.
(67) Sasongko, M. I. N.; Puspitasari, P.; Yazirin, C.; Tsamroh, D. I.; Risdanareni, P. Morphology and Phase Identification of Micron to Nanosized Manganese Oxide (MnO) with Variations in Sintering Time; East Java, Indonesia, 2017; p 020037. https://doi.org/10.1063/1.5003520.
(68) Salasin, J.; Rawn, C. Structure Property Relationships and Cationic Doping in $[Ca_{24}Al_{28}O_{64}]^{4+}$ Framework: A Review. *Crystals* **2017**, *7* (5), 143. https://doi.org/10.3390/cryst7050143.
(69) Li, J.; Hayashi, K.; Hirano, M.; Hosono, H. Sustainable Thermionic O^- Emission from Stoichiometric $12CaO{\bullet}7Al_2O_3$ with Nanoporous Crystal Structure. *Journal of The Electrochemical Society* **2009**, *156* (1), G1. https://doi.org/10.1149/1.2999055.